

Dynamical Properties of Excitable Membranes

Douglas A. Baxter and John H. Byrne

The nervous system functions to encode, process, store and transmit information. To perform these tasks, neurons have evolved sophisticated means of generating electrical and chemical signals. Chapters 4, 5 and 6 describe several aspects of intracellular chemical signaling mechanisms (e.g., second-messenger cascades and genetic-regulatory networks) and Chapters 12, 13, 16 and 17 describe several aspects of electrical signaling in neurons (e.g., the membrane potential, the action potential and synaptic transmission). The goals of this chapter are to provide a more detailed mathematical description of neuronal excitability and to introduce several mathematical tools based upon the theory of nonlinear dynamical systems that can be used to analyze neuronal excitability. These mathematical tools (e.g., phase plane analysis, bifurcation theory) provide graphical or geometric representations of the system dynamics and can be used to understand, predict and interpret biophysical features such as threshold phenomena, oscillatory and bursting behavior, as well as the mechanisms of bistability and hysteresis. Such analyses can provide novel insights into the capabilities of individual neurons to process and store information.

THE HODGKIN-HUXLEY MODEL

Since 1952, the understanding and methods for studying the biophysics of excitable membranes have been profoundly influenced by the pioneering work of Alan Hodgkin and Andrew Huxley. Using the techniques of voltage clamping, which had recently been developed by Cole (1949) and Marmont (1949) and improved upon by Hodgkin et al. (1952) (see also Chapters 12 and 13), Hodgkin and Huxley characterized the time- and voltage-dependency of the ionic

conductances that underlie an action potential in the squid giant axon (Hodgkin et al., 1952; Hodgkin and Huxley, 1952a–c). In addition, they developed a cogent mathematical model that accurately predicted the waveform of the action potential and several other physiological properties such as the refractory period, propagation of the action potential along an axon, anode break excitation and accommodation (Hodgkin and Huxley, 1952d). In biology, quantitatively predictive theories are rare, and this work stands out as one of the most successful combinations of experimental and computational approaches to understanding a fundamentally important issue in neuroscience. For their seminal work on neuronal excitability, Hodgkin and Huxley received the Nobel Prize in Physiology or Medicine in 1963.

To view biographical information about Hodgkin and Huxley and other Nobel laureates, visit the Nobel Prize web site (<http://www.nobel.se/nobel>). The lectures that Hodgkin (1964) and Huxley (1964) delivered when they received the Nobel Prize were published in 1964. In addition, Hodgkin (1976, 1977) and Huxley (2000, 2002) published informal narratives describing events surrounding these studies, and others have reviewed the work of Hodgkin and Huxley from a historical perspective (Catterall et al., 2012; Cole, 1968; Hille, 2001; Huang, 2012; Moore, 2010; Nelson, 2011; Nelson and Rinzel, 1998; Rinzel, 1990; Schwiening, 2012; Vandenberg and Waxman, 2012). Their empirical studies and quantitative model remain influential to the present day and provide an analytical framework for investigating and modeling a large class of diverse membrane phenomena. The first half of this chapter will review the steps taken by Hodgkin and Huxley to derive a mathematical description of neuronal excitability. The second half of this chapter will discuss applying techniques from the mathematical field of

nonlinear dynamics to the analysis of neuronal excitability.

Perhaps the best way to begin a discussion of the Hodgkin-Huxley (HH) model is to analyze the *equivalent electrical circuit* employed by Hodgkin and Huxley to represent a patch of membrane (Fig. 14.1). In this approach, the membrane is considered to be an electrical circuit composed of a capacitive element (C_m) in parallel with conductances (g), which are in series with a battery. The capacitive element represents the dielectric properties of the lipid bilayer of biological membranes. The conductances represent channels in the membrane through which ions can pass (see Chapters 11 and 13) and the batteries represent the electrochemical potential gradient that is associated with a given species of ion (see Chapter 12). In the equivalent circuit, the current that flows across the membrane (I_m) has two major components, one associated with charging the membrane capacitance (I_{Cm}) and one associated with the movement of ions across the membrane (I_{ionic}). Thus:

$$I_m = I_{Cm} + I_{ionic} = C_m \frac{dV_m}{dt} + I_{ionic} \quad (14.1)$$

where V_m is potential across the membrane, and t is time.

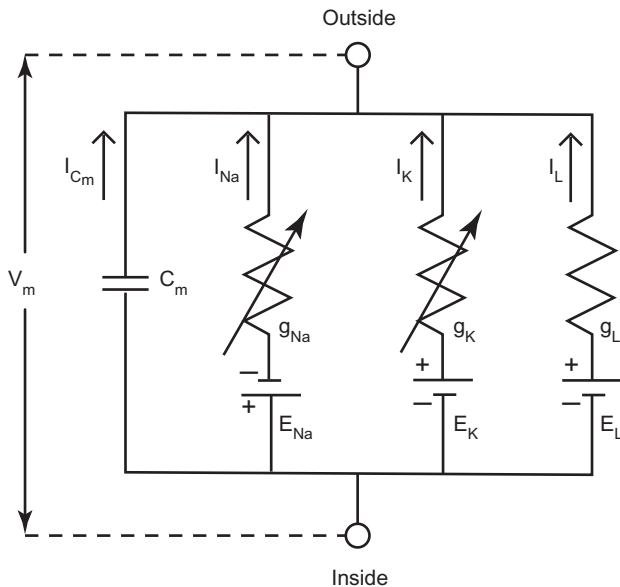


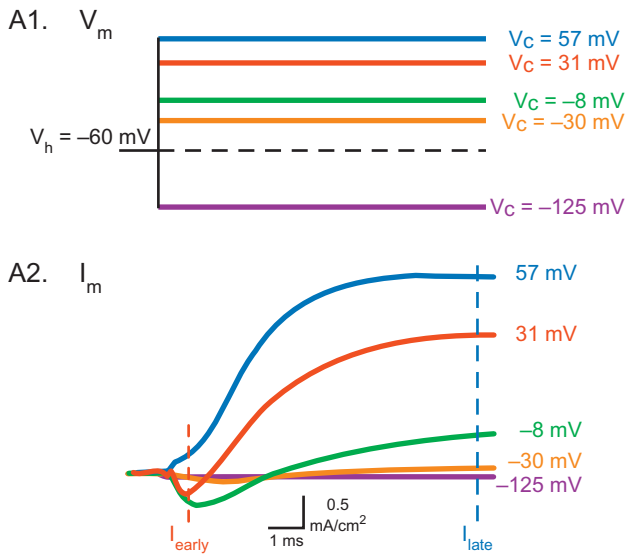
FIGURE 14.1 Equivalent electrical circuit proposed by Hodgkin and Huxley for a patch of squid giant axon. The electrical circuit has four parallel branches. The capacitive branch (C_m) represents the dielectric properties of the membrane. The variable resistors (resistors with arrows) represent voltage- and time-dependent conductances of Na^+ (g_{Na}) and K^+ (g_{K}), whereas the leakage conductance (g_{L}) is constant. Each conductance element is in series with a battery (E_{Na} , E_{K} , E_{L}) that represents its electromotive force. Adapted from Hodgkin and Huxley (1952d).

Separating the Membrane Current into its Major Components

As a first step in their analysis, Hodgkin and Huxley separated the membrane current into its major components (i.e., the capacitive, I_{Cm} , and ionic, I_{ionic} , currents). It was the voltage-clamp technique that provided the method for this separation. By using a feedback circuit (see Chapter 12), the voltage-clamp technique maintains (i.e., “clamps”) the membrane potential at a designated voltage (Hodgkin et al., 1952). In a typical experiment (Fig. 14.2), the membrane potential was held at voltage (i.e., the *holding voltage*, V_h), which was often near the resting potential of the neuron, and voltage-clamp commands (i.e., the *command voltage*, V_c) stepped the membrane potential from V_h to various depolarized or hyperpolarized levels for a few milliseconds, and then back to V_h . The stepwise depolarizations (or hyperpolarizations) of the membrane have two advantages for measuring ionic current. First, except for the brief moment of transition between V_h and V_c , the membrane potential is constant (i.e., $dV_m/dt = 0$). Thus, the capacitive current is eliminated and the ionic current can be measured in isolation. Second, by keeping the voltage constant, the time dependency of the ionic currents can be measured.

The voltage-clamp technique provides a quantitative measure of the ionic currents that flow through an excitable membrane such as the squid giant axon. An example of the types of membrane currents that were recorded by Hodgkin and Huxley is presented in Fig. 14.2A (see also Chapters 12 and 13). When the membrane potential was depolarized, a transient inward current (i.e., the flow of positive charge into the cell) was observed. This transient inward current (i.e., I_{early}) was followed by a sustained outward current (i.e., I_{late}), which represents the flow of positive charge out of the cell. The time course and magnitude of these ionic currents depended markedly on the magnitude of the depolarizing step (i.e., V_c). For example, the amplitude of I_{early} increased and then decreased as V_c became more positive, whereas I_{late} increased monotonically with V_c (Fig. 14.2B). Because of the voltage-dependency of some membrane currents, the underlying channels, through which the ions flow, are often referred to as *voltage-gated channels*.

The second step in the analysis was to separate the complex ionic current into its components. By altering the ionic composition of the external solutions (e.g., substituting choline for Na^+) (Hodgkin and Huxley, 1952a), the inward current (i.e., I_{early}) was eliminated (Fig. 14.3), leaving only outward current (i.e., I_{late}), which was assumed to be carried by K^+ (Huxley 1951). Thus, the ionic current was subdivided into two



B. Current - Voltage (I-V) Relationships

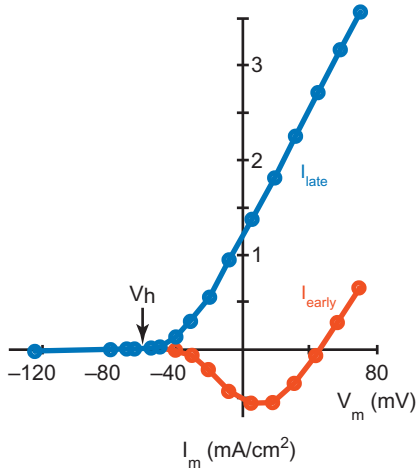


FIGURE 14.2 Membrane currents (I_m) recorded with voltage clamp of squid axon. Data are from an experiment by [Hodgkin et al. \(1952\)](#) (i.e., axon 41 at 3.8°C). **A1:** In this simple voltage-clamp protocol, the membrane potential (V_m) was held near its rest potential, which is taken to be -60 mV (i.e., $V_h = V_m = -60$ mV). Voltage-clamp commands (V_c) were used to step the membrane potential to various hyperpolarized and depolarized potentials, which are indicated next to each trace. (Hodgkin and Huxley used a different convention for labeling membrane potentials and displaying currents; see [Box 14.1](#) for an explanation. In this and all subsequent figures, the data have been modified to reflect modern conventions.) **A2:** Responses elicited by a series of voltage-clamp steps. Successive current traces have been superimposed. Inward current is indicated by a downward deflection and outward current is indicated by an upward deflection. (Only the response immediately prior to and during the initial phase of the voltage-clamp step is shown. The response at the end of the voltage-clamp step is not illustrated.) The time course, direction and magnitude of I_m vary with V_m . **B:** Current-voltage relation (i.e., I - V plot) from voltage-clamp experiment that is illustrated in Panel A. (Additional data points are included in the I - V plot that were not illustrated in Panel A.) The magnitude of the currents at 0.5 and 8 ms (I_{early} and I_{late} , respectively) are plotted as functions of V_m . Adapted from [Hodgkin et al. \(1952\)](#).

primary components: one carried by Na^+ (I_{Na}) and another carried by K^+ (I_{K}). In addition, there is a small component that is referred to as the *leakage current* (I_{L}), which represent ions flowing through non-voltage-gate channels. Thus, the total ionic current was expressed as:

$$I_{\text{ionic}} = I_{\text{Na}} + I_{\text{K}} + I_{\text{L}} \quad (14.2)$$

In addition to separating the ionic current into its components, it was necessary to determine the relationship between ionic current and membrane potential at a constant permeability. To examine this issue, Hodgkin and Huxley developed a voltage-clamp protocol that measured what they referred to as the *instantaneous current-voltage (I-V) relationship* ([Hodgkin and Huxley, 1952b](#)). In this protocol, two voltage-clamp commands were applied to the axon ([Fig. 14.4](#)). The first voltage-clamp command (V_1) was brief and had a fixed amplitude, whereas the amplitude of the second voltage-clamp step (V_2) was varied. V_1 served to activate (i.e., open) the Na^+ channels (i.e., the channels that mediate I_{early} in [Fig. 14.2](#)). After the Na^+ channels were activated by V_1 , the membrane potential was suddenly stepped to V_2 and the current (I_2) was measured within the first few microseconds of V_2 (i.e., at the instant the membrane potential changed from V_1 to V_2). (Because I_2 is measured at the “tail end” of V_1 , such currents are also referred to as *tail currents*.) The purpose of this protocol was to measure the current without time-dependent influences. Immediately after the step from V_1 to V_2 , the level of activation (and inactivation) is constant because it has not yet had time to change. Thus, only the driving force $\Delta V = (V_m - E_{\text{ion}})$, where $V_m = V_2$, differs for different values of V_2 . The results indicated that the I - V relationship of I_2 was approximately linear. The instantaneous I - V relationship of K^+ channels was also studied, and a similar linear relationship was observed. These results indicated that under normal ionic conditions the flow of ionic current in open Na^+ and K^+ channels obeys *Ohm's Law* (i.e., $\Delta V = I \times R$, where $G = 1/R$, and R stands for resistance and G for its inverse, conductance). It follows, therefore, that by using their empirical measurements of I_{Na} and I_{K} , Hodgkin and Huxley were able to determine g_{Na} and g_{K} (see the following).

Ohm's Law implies that the individual ionic currents in [Eq. 14.2](#) were proportional to the conductance (i.e., g) times the *driving force* (i.e., the difference between the membrane potential, V_m , and the Nernst potential, E_{ion} , for a given ion species), resulting in a general equation for an ionic current of the form:

$$I_{\text{ion}}(V_m, t) = g_{\text{ion}}(V_m, t)(V_m - E_{\text{ion}}) \quad (14.3)$$

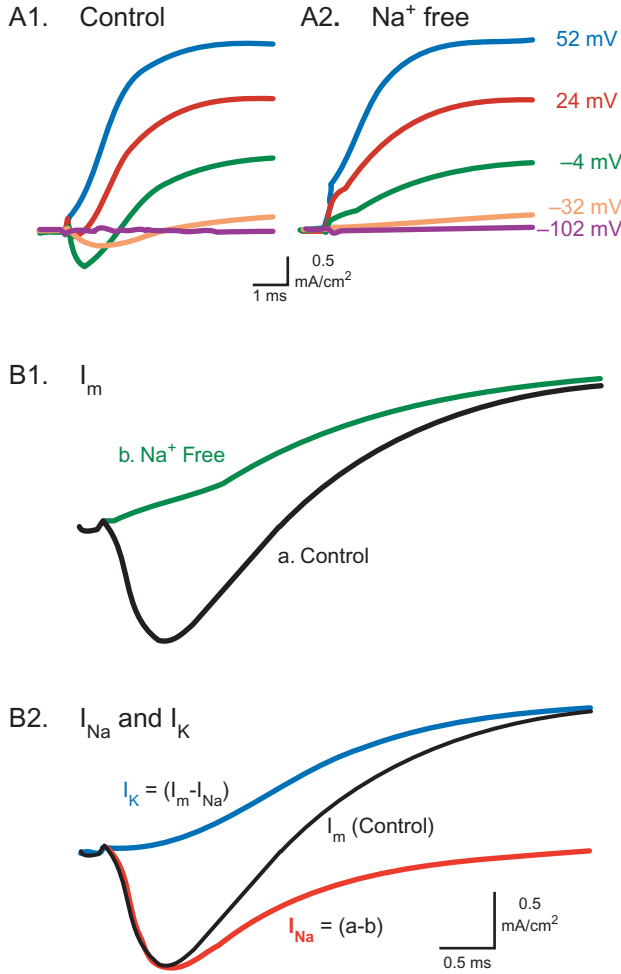


FIGURE 14.3 Separation of membrane current (I_m) into components carried by Na^+ (I_{Na}) and K^+ (I_{K}). Data are from an experiment by Hodgkin and Huxley (1952a) (axon 21 at 8.5°C). **A:** Total membrane currents (I_m) were measured in Control (**A1**) and Na^+ -free (**A2**) solutions. The membrane potential was held at -60 mV, and was stepped to the various potentials indicated to the right of each trace. (Only the response immediately prior to and during the voltage-clamp step is illustrated.) In control solutions, command voltages that depolarized the membrane potential elicited an inward current followed by an outward current. After the Na^+ in the solution was replaced with impermeant choline ions, the inward component of I_m was abolished and only the outward component remained. **B1:** Enlarged view of the membrane currents elicited by the voltage-clamp step to -4 mV, in Panel A. Membrane currents were first elicited in Control solution (i.e., trace a) and again after removal of Na^+ (trace b), which blocked the inward component of I_m . **B2:** Subtracting the response in the Na^+ -free solution from the response in control solution (i.e., trace a - trace b) revealed the amplitude and time course of the Na^+ -dependent component of I_m (i.e., I_{Na}). Similarly, I_{K} could be isolated by subtracting I_{Na} from I_m . Adapted from Hodgkin and Huxley (1952a).

where $I_{\text{ion}}(V, t)$ is the current created by the movement of a given species of ion across the membrane, $g_{\text{ion}}(V, t)$ represents the voltage- and time-dependent conductance (i.e., permeability) of the membrane to that ionic

species, and E_{ion} is the Nernst potential of the ion (see Chapter 12). Thus, I_{Na} , I_{K} and I_{L} were described by:

$$I_{\text{Na}}(V_m, t) = g_{\text{Na}}(V_m, t)(V_m - E_{\text{Na}}) \quad (14.4)$$

$$I_{\text{K}}(V_m, t) = g_{\text{K}}(V_m, t)(V_m - E_{\text{K}}) \quad (14.5)$$

$$I_{\text{L}} = g_{\text{L}}(V_m - E_{\text{L}}) \quad (14.6)$$

By substituting Eq. 14.2 into Eq. 14.1, the description of membrane current becomes:

$$I_m = C_m \frac{dV_m}{dt} + I_{\text{Na}} + I_{\text{K}} + I_{\text{L}} \quad (14.7)$$

Finally, Eq. 14.7 can be expanded by including Eqs. 14.4, 14.5 and 14.6, and becomes:

$$I_m = C_m \frac{dV_m}{dt} + g_{\text{Na}}(V_m, t)(V_m - E_{\text{Na}}) + g_{\text{K}}(V_m, t)(V_m - E_{\text{K}}) + g_{\text{L}}(V_m - E_{\text{L}}) \quad (14.8)$$

The final stage of the analysis was to characterize the active conductances (i.e., $g_{\text{Na}}(V, t)$ and $g_{\text{K}}(V, t)$).

Analyzing the Time and Voltage Dependency of Ionic Conductances

To analyze the ionic conductances, it was first necessary to devise a method for obtaining measures of g_{Na} and g_{K} . The linear nature of the instantaneous I-V relationship for I_{Na} and I_{K} (see above) indicated that these ionic currents and their underlying ionic conductances were related by Ohm's Law. This provided Hodgkin and Huxley with the means of calculating g_{Na} and g_{K} . From Eqs. 14.4 and 14.5, it is possible to define ionic conductances as:

$$g_{\text{Na}}(V_m, t) = \frac{I_{\text{Na}}(V_m, t)}{V_m - E_{\text{Na}}} \quad (14.9)$$

$$g_{\text{K}}(V_m, t) = \frac{I_{\text{K}}(V_m, t)}{V_m - E_{\text{K}}} \quad (14.10)$$

Thus, changes in the conductances g_{Na} and g_{K} during a voltage-clamp step could be calculated by applying Eqs. 14.9 and 14.10 to separated ionic currents. Fig. 14.5 illustrates data obtained by Hodgkin and Huxley in which the magnitude and time course of g_{K} and g_{Na} were calculated for two different voltage-clamp steps. As discussed in Chapter 12, these conductances have several striking properties. First, the magnitude of the conductances increases with more positive values of V_m . Second, the rising phase of the conductances become more rapid with increasing V_m . Third, there is delay in the onset of the change in the conductances, particularly for g_{K} . Finally, the increase in g_{Na} is transient, whereas the increase in g_{K} is not.

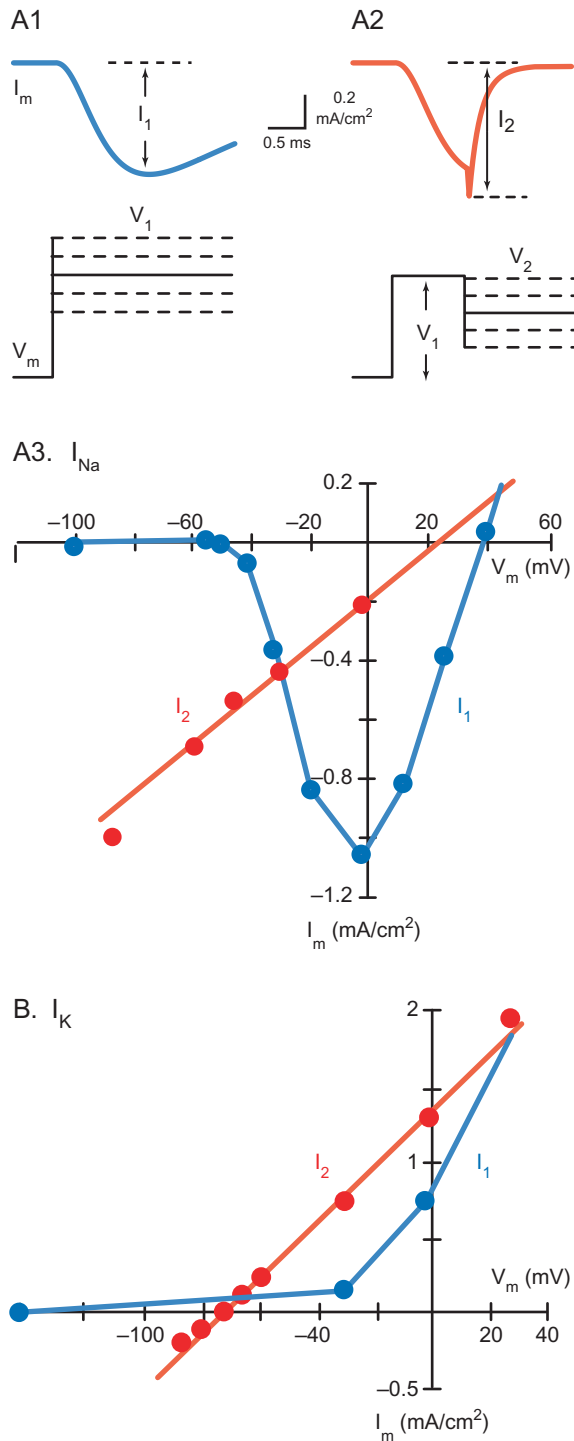


FIGURE 14.4 Instantaneous current-voltage (I-V) relations for the early and late components of I_m (i.e., I_{Na} and I_K , respectively). **A1:** In a simple voltage-clamp protocol, the membrane potential is stepped from a holding potential to various depolarized (or hyperpolarized) command voltages (V_1), which activate ion channels and elicit the flow of membrane currents (I_1). **A2:** To measure the instantaneous I-V relation, two command-voltage steps are used. The first voltage-clamp step (V_1) is to a fixed potential. The second voltage-clamp step (V_2) varied between -100 mV and 50 mV. The instantaneous current (I_2) is measured immediately (i.e., within ~ 30 μ s) of

To explain these experimental data, Hodgkin and Huxley suggested a model that could account for the voltage- and time-dependent properties of g_K and g_{Na} . This model is often referred to as the *gate model* (Fig. 14.6; see also Chapters 11–13). The model assumes that the macroscopic conductances as measured with the voltage-clamp procedure arise from the combined effects of many individual ion channels, each with a microscopic conductance to a specific species of ion (i.e., K^+ or Na^+). Each individual channel has one or more “gates” that regulate the flow of ions through the channel. Each gate can be in one of two states: open or closed. When all the gates for a particular channel are open, ions can pass through the channel (i.e., the single channel conductance is >0). If any of the gates are closed, ions cannot pass through the channel (i.e., the single channel conductance is 0). The status of a gate (i.e., open vs. closed) was assumed to be controlled by distribution of one or more charged “particles” within the membrane (i.e., *gating particles* or *gating charges*). These gating particles act as “molecular voltmeters,” and as the electrical field across the membrane changes, the distribution of these gating particles is altered such that the gates transition between states. A gate is open only when all of the particles that are associated with the gate are in a permissive state. The possible molecular structures responsible for gating particles are described in Chapters 11–13.

the second voltage-clamp step. **A3:** Current-voltage relationships for the early inward component of I_m (i.e., I_{Na}). The current-voltage relation of the maximum inward current during a single voltage-clamp step (i.e., I_1 in Panel A) is extremely nonlinear (blue curve). In contrast, the current-voltage relation of the instantaneous current at the beginning of the second voltage-clamp step (i.e., I_2 in Panel B) is approximately linear (red curve). Data are from an experiment by Hodgkin and Huxley (1952b) (i.e., axon 31 at 4°C). **B:** Current-voltage relationships for the late outward component of I_m (i.e., I_K), which were measured while the axon was bathed in Na^+ -free saline. The current-voltage relationship of current measured ~ 0.6 ms after the beginning of the first voltage-clamp step (i.e., I_1 vs. V_1) is nonlinear (blue trace), whereas the current-voltage relationship of the instantaneous current (i.e., I_2) is approximately linear (red trace). Data are from an experiment by Hodgkin and Huxley (1952b) (axon 26 at 20°C). The linear I-V relationships of the instantaneous currents (i.e., I_2) was in striking contrast to the extremely nonlinear I-V relationships that were obtained when the currents were measured at later intervals (i.e., I_1). The curvature of the I_1 I-V relationships (i.e., blue traces in Panels A3 and B) reflects the voltage- and time-dependent opening of Na^+ and K^+ channels. In contrast, the linear nature of the instantaneous current-voltage relationships (i.e., red traces in Panels A3 and B) indicate that the flow of ionic currents in open channels obey Ohm’s law. Adapted from Hodgkin and Huxley (1952b).

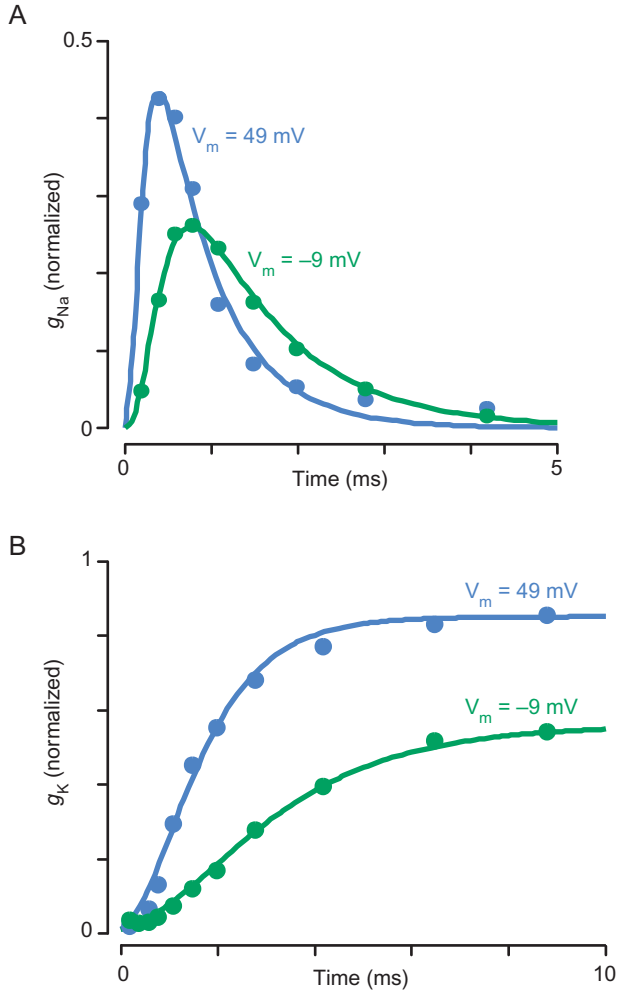


FIGURE 14.5 Experimental voltage-clamp data illustrating the voltage- and time-dependent properties of the g_{Na} (A) and g_K (B). By recording membrane currents in solutions of different ionic composition (e.g., normal sea water vs. Na^+ -free sea water), Hodgkin and Huxley (1952a) were able to isolate I_{Na} and I_K (see also Fig. 14.3 and Chapters 12 and 13). The conductances were calculated using Eqs. 14.9 and 14.10. Although Hodgkin and Huxley examined a wide range of membrane potentials, the results from only two voltage-clamp steps are illustrated. The blue traces are responses elicited by a command voltage (V_c) to 49 mV and the green traces are responses elicited during a voltage-clamp step to -9 mV. The voltage-clamp steps are not illustrated, but they begin at $t=0$ and extend beyond the end of the illustrations. The filled circles are data from an experiment by Hodgkin and Huxley (axon 17) and the solid lines are best-fit curves for Eqs. 14.24 and 14.32. Adapted from Hodgkin and Huxley (1952d).

Mathematically, the voltage dependence of channel opening (and closing) can be derived using the Boltzmann equation of statistical mechanics, which describes the equilibrium distribution of independent particles in force fields. From the Boltzmann principle, the proportion of gating particles that are at a location associated with a *permissive state* (P_i) is related to the

proportion of gating particles in *nonpermissive* locates (P_o) by the function:

$$\frac{P_i}{P_o} = \exp\left(\frac{w + zeV}{kT}\right) \quad (14.11)$$

where w is the work required to move the gating particle from the nonpermissive state to the permissive state, z is the valence of the particle, e is the elementary charge of the particle, V is the potential difference between the inside and outside of the membrane, k is Boltzmann's constant, and T is the absolute temperature. Since $P_i + P_o = 1$, Eq. 14.11 can be rearranged to give the proportion of gating particles in the permissive state as a function of voltage:

$$P_i = \frac{1}{1 + \exp\left(\frac{-(w + zeV)}{kT}\right)} \quad (14.12)$$

Eq. 14.12 quantifies the voltage dependence of gating in the system and is sometimes referred to as the *activation function of a channel*. As V increases in Eq. 14.12 (i.e., the membrane potential is depolarized), the proportion of gating particles in the permissive state approaches unity (i.e., $P_i \rightarrow 1$). With an increasing proportion of gating particles in the permissive state, a greater number of channels are likely to be open, and thus, the macroscopic membrane conductance will increase. Fig. 14.7 illustrates semilogarithmic plots of Eq. 14.12 that are superimposed on the maximum values of g_{Na} and g_K that were measured during a voltage-clamp experiment. The two curves are very similar in shape. One of the most striking properties of the curves is the extreme steepness of the relation between ionic conductance and membrane potential. At low depolarizations (i.e., near the resting potential), the curves approach straight lines. Because the ordinate is plotted on a logarithmic scale, this means that the peak conductances increase exponentially with membrane depolarization, until at high depolarizations, the curves reach a maximal value and flatten (i.e., saturate). These maximal conductances are denoted \bar{g}_{Na} and \bar{g}_K . To describe the time- and voltage-dependency of g_{Na} and g_K (see Fig. 14.5), \bar{g}_{Na} and \bar{g}_K must be multiplied by coefficients, which represent the fraction of the maximum conductances expressed at any given time and at any given membrane potential. Thus, g_{Na} and g_K can be written in a general form as:

$$g_{Na}(V_m, t) = y_{Na}(V_m, t)\bar{g}_{Na} \quad (14.13)$$

$$g_K(V_m, t) = y_K(V_m, t)\bar{g}_K \quad (14.14)$$

where y_{Na} and y_K are functions of one or more gating variables (y_i) that vary between zero and one.

The excellent agreement between the observed voltage dependency of g_{Na} and g_K and the Boltzmann

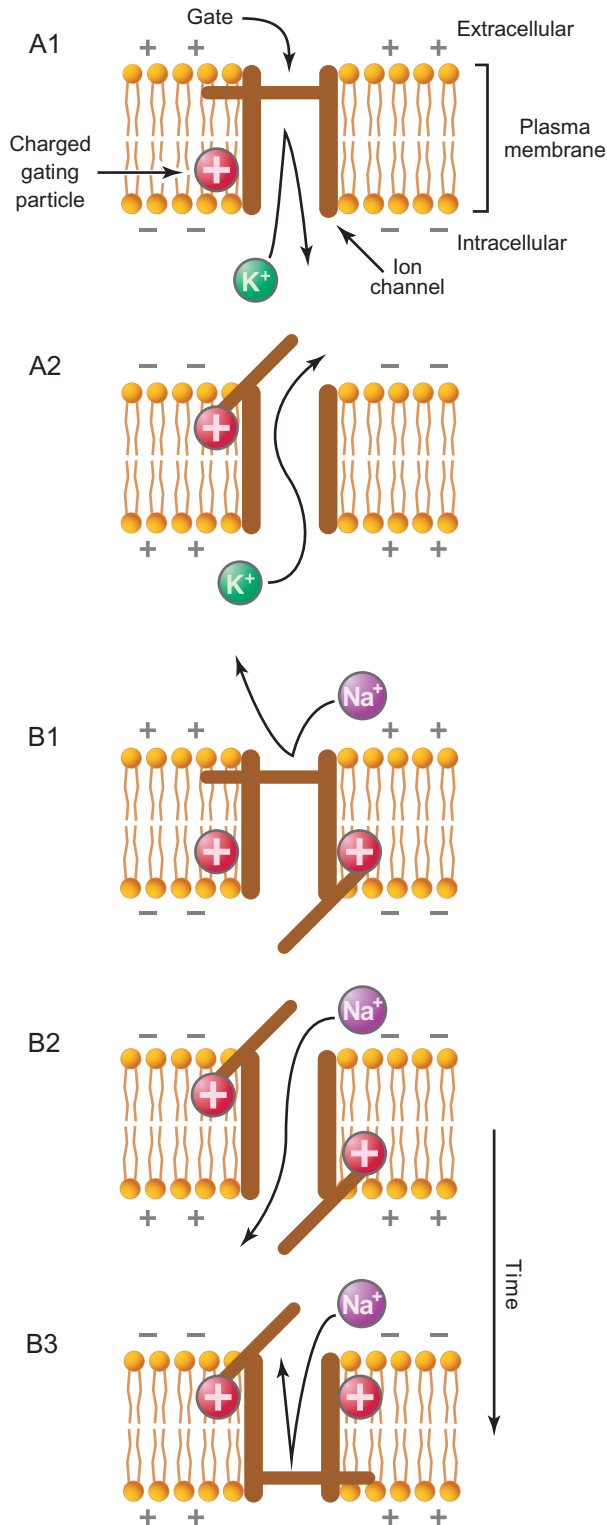


FIGURE 14.6 Schematic representation of the gate model that was proposed by Hodgkin and Huxley (1952d). The gate model assumes that many individual ion channels, each with a small ionic conductance, determine the behavior of the macroscopic membrane conductance. The ion channels have “gates” that are controlled by voltage-sensitive gating charges or particles. If the gating particles are in the permissive state, then the gates are open and ions can pass

equation (i.e., Fig. 14.7) lent support to Hodgkin and Huxley’s proposition that changes in ionic permeability depended on the movement of some component of the membrane that behaved as though it were a charged particle. In addition to providing a possible mechanism for the voltage dependency (i.e., the nonlinear I-V relations in Fig. 14.2) of membrane conductance, the

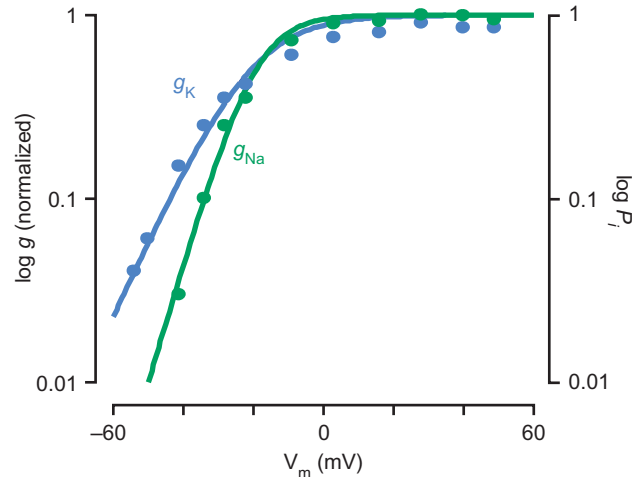


FIGURE 14.7 Voltage dependence of ionic conductances. The maximum g_{Na} and g_K were measured at several different membrane potentials under voltage clamp. The filled circles represent data from an experiment by Hodgkin and Huxley (axon 17) and the solid lines represent best-fit curves of the form given in Eq. 14.12. (The calculations assumed $w = 0$.) The most striking feature of the conductances is the extreme steepness of the relation between ionic conductance and the membrane potential. A depolarization of only ~ 4 mV can increase g_{Na} by e-fold ($e \approx 2.72$), while the corresponding figure for g_K is ~ 5 mV. Adapted from Hodgkin and Huxley (1952a).

through the channel. Otherwise, the gates are closed and passage of ions through the channel is blocked. In this example, each gate is regulated by a single gating particle and the gating particles are assumed to be positively charged. Other scenarios are possible, however. **A:** K⁺ channels are regulated by a single activation gate, which is embodied in the HH model as n (see Eq. 14.33). At the resting potential (as indicated by the minus signs, “−”, on the intracellular surface and the plus signs, “+”, on the extracellular surface), the gating particles are primarily distributed at locations within the membrane that are nonpermissive, i.e., the gate is closed (**A1**). As the membrane potential is depolarized (**A2**; note translocation of “−” and “+” signs), the probability increases that a gating particle will be located in a position that is permissive, i.e., the gate is open (i.e., activation). Potassium ions (K⁺) can flow through the open channel. **B:** Na⁺ channels are regulated by two gates: an activation gate and inactivation gate. These two gates are embodied in the HH model as m and h , respectively (see Eq. 14.25). Unlike the activation gate, the inactivation gate is normally open at the resting potential (**B1**). Upon depolarization (**B2**), the probability increases that the activation gate will open, whereas the probability that the inactivation gate will remain open decreases. While both gates are open, Na⁺ passes through the channel. As the depolarization continues, however (**B3**), the inactivation gate closes and ions can no longer pass through the channel (i.e., inactivation).

gate model also offered a possible explanation for the time dependency of ionic conductances (Fig. 14.8). The gate model assumed that the rate of change in an ionic conductance following a step depolarization was governed by the rate of redistribution of the gating particles within the membrane and that the transitions between *permissive* (i.e., open or activated) and *non-permissive* (i.e., closed or deactivated) states can be described by the following first-order kinetic model:

$$(1 - y) \xrightleftharpoons[\beta_y(V_m)]{\alpha_y(V_m)} y \quad (14.15)$$

where y is the probability of finding a single gating particle in the permissive state, $(1 - y)$ is the probability of finding the particle in the nonpermissive state, and $\alpha_y(V_m)$ and $\beta_y(V_m)$ are voltage-dependent rate constants describing the rate at which a particle moves from nonpermissive to permissive states (α_y) and from permissive to nonpermissive states (β_y). If a gate is regulated by a single particle, then the probability that the gate will open over a short interval of time is proportional to the probability of finding the gate closed multiplied by the opening rate constant (i.e., $\alpha_y(V_m)(1 - y)$). Conversely, the probability that the gate will close over a short interval of time is proportional to the probability of finding the gate open multiplied by the closing rate constant (i.e., $\beta_y(V_m)y$). The rate at which the open probability for a single gating particle changes following a change in membrane potential is given by the difference of these two terms:

$$\frac{dy}{dt} = \alpha_y(V_m)(1 - y) - \beta_y(V_m)y \quad (14.16)$$

The first term in Eq. 14.16 (i.e., $\alpha_y(V_m)(1 - y)$) describes the opening (i.e., *activation*) of the gate and the second term (i.e., $\beta_y(V_m)y$) describes the closing (i.e., *deactivation*) of the gate.

Although y is usually taken to represent the probability of finding a single gate in the open state, it can also be interpreted as the fraction of open gates in a large population of gates, and $(1 - y)$ would be the fraction of gates in the closed state. If the membrane potential is voltage clamped to some fixed value, then the fraction of gates in the open state will eventually reach a steady-state value (i.e., $dy/dt = 0$) as $t \rightarrow \infty$. Solving Eq. 14.16 for the steady-state value ($y_\infty(V_m)$) yields:

$$y_\infty(V_m) = \frac{\alpha_y(V_m)}{\alpha_y(V_m) + \beta_y(V_m)} \quad (14.17)$$

During a voltage-clamp step, the time course for approaching this steady state (i.e., the solution of a

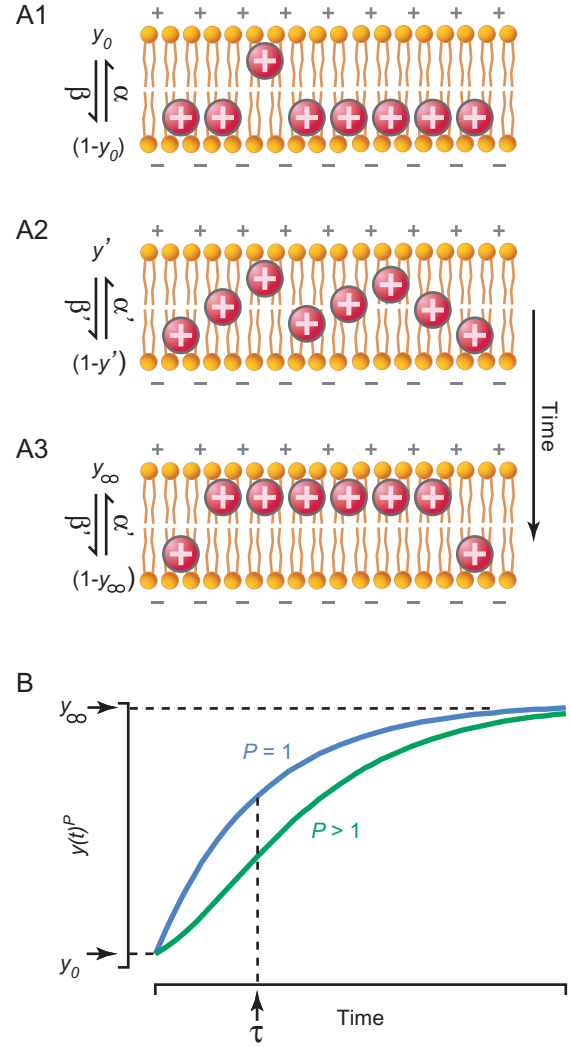


FIGURE 14.8 Kinetics of the increasing probability of channel activation during a voltage-clamp step. **A:** Changes in the membrane potential alter the distribution of gating particles within the membrane. In this example, gating particles are assumed to have a positive charge and the permissive site for opening a gate is assumed to be at the outer surface of the membrane (see Fig. 14.6). **A1:** At the resting potential, the probability of a gating particle being in a permissive state (y_0) is low, whereas the probability of a gating particle being in a nonpermissive state ($1 - y_0$) is high. **A2:** Immediately following a depolarization (note the translocation of the “-” and “+” signs), the gating particles begin to redistribute. The rate of movement of the gating particles within the membrane is described by Eq. 14.16. The voltage-dependent rate constant α represents the rate at which particles move from the inner to outer surface (i.e., from non-permissive to permissive states), and β is the rate of reverse movement. **A3:** Eventually, the distribution reaches a steady state in which the probability of a gating particle being in a permissive state has increased (y_∞). **B:** The kinetics of the redistribution of gating particles is described by Eq. 14.18. If a channel is controlled by a single gating particle (i.e., $P = 1$ in Eq. 14.20), then the solution is a simple exponential. If a channel is controlled by several identical and independent gating particles (i.e., $P > 1$), then a delay is noted in the change in conductance.

first-order kinetic expression like Eq. 14.16) is described by a simple exponential function:

$$y(t) = y_\infty(V_c) - (y_\infty(V_c) - y_0)\exp^{-t/\tau_y(V_c)} \quad (14.18)$$

where y_0 is the initial value of y (i.e., the value of y at the holding potential, V_h) and the time constant, $\tau_y(V_m)$, is given by:

$$\tau_y(V_m) = \frac{1}{\alpha_y(V_m) + \beta_y(V_m)} \quad (14.19)$$

If P independent and identical gating particles are involved in gating a channel, then the probability that all of the particles will simultaneously be in the permissive state is the product of their individual probabilities (i.e., $y(t)^P$). Thus, by substituting Eq. 14.19 and by including the possibility of more than one gating particle, the time course for approaching the steady state becomes:

$$y(t)^P = (y_\infty(V_c) - (y_\infty(V_c) - y_0)\exp^{-(\alpha_y(V_c) + \beta_y(V_c))t})^P \quad (14.20)$$

As the number of gating particles increases (i.e., $P > 1$), a delay and a sigmoidal rising phase are introduced to the time course of $y(t)^P$ (Fig. 14.8B).

Instead of using the rate constants α_y and β_y , Eq. 14.16 can be written in terms of the steady-state value $y_\infty(V_m)$ (i.e., Eq. 14.17) and the voltage-dependent time constant (i.e., Eq. 14.19). Thus, Eq. 14.16 becomes:

$$\frac{dy}{dt} = \frac{y_\infty(V_m) - y}{\tau_y(V_m)} \quad (14.21)$$

Eq. 14.21 indicates that for a fixed voltage (V_m), the gating particle (y) approaches the steady-state value ($y_\infty(V_m)$) exponentially with the time constant $\tau_y(V_m)$. Although Eqs. 14.16 and 14.21 are equivalent, Eq. 14.21 is simpler to interpret and is more conveniently fit to experimental data. In addition, from Eqs. 14.17 and 14.19, it is possible to calculate α_y and β_y from experimental data:

$$\alpha_y(V_m) = \frac{y_\infty(V_m)}{\tau_y(V_m)} \quad (14.22)$$

$$\beta_y(V_m) = \frac{1 - y_\infty(V_m)}{\tau_y(V_m)} \quad (14.23)$$

where y_∞ and τ_y are measured empirically (see the following).

In the discussion provided above, the descriptions of gating particles (i.e., Eqs. 14.13–14.21) have been presented using generalized notation that can be applied to a wide variety of conductances. The key remaining tasks in the development of the HH model

are determining the number and type of gating particles that regulate g_{Na} and g_K and quantitatively describing the voltage dependency of the rate constants that govern these gating particles. In brief, this was done by measuring the $\tau_y(V_m)$ and $y_\infty(V_m)$ from the time records of g_{Na} and g_K (e.g., Fig. 14.5) and then calculating the rate constants using Eqs. 14.22 and 14.23. The values for the rate constants were plotted as functions of membrane potential and the data were fit with empirically derived exponential functions (see the following).

CHARACTERIZING THE Na^+ CONDUCTANCE

As illustrated in Fig. 14.5A, the dynamics of g_{Na} are complex. This led Hodgkin and Huxley to postulate that g_{Na} was regulated by two types of gates. One gate regulated the activation of g_{Na} and was termed m , and the other gate regulated inactivation and was termed h . To analyze the empirical voltage-clamp data and extract values for g_{Na} , τ_m , τ_h , and P (see Eqs. 14.13, 14.20, 14.22 and 14.23), an exponential function was fit to the time course of g_{Na} during voltage-clamp steps to various membrane potentials. Hodgkin and Huxley used an exponential function to fit the time course of g_{Na} during a voltage-clamp step (Fig. 14.9A):

$$g_{\text{Na}}(t) = g'_{\text{Na}}(V_c)(1 - \exp^{-t/\tau_m})^3 \exp^{-t/\tau_h} \quad (14.24)$$

where $g'_{\text{Na}}(V_c)$ is the value that g_{Na} would attain during the voltage-clamp step if h remained at its resting value (i.e., $h = 1$). This extrapolation is illustrated in Fig. 14.10. During the voltage-clamp step to V_c , m changes from its resting value, which in this example is 0, to a new steady-state level, which in this example is 1 (the curve labeled m^3). Conversely, the resting level of h in this example is 1, and during the voltage-clamp step to V_c , h approaches a new steady-state value, which in the example is 0 (curve labeled h). In the absence of h (i.e., the curve labeled m^3) the activation of g_{Na} attains a higher level and is maintained as compared to when h is included in the calculation (i.e., the curve labeled m^3h). The multiplicative interaction of the activation and inactivation gating variables (i.e., m and h) produces the transient response of g_{Na} during a voltage-clamp step and reduces the apparent magnitude of activation g_{Na} . The best fit of Eq. 14.24 to voltage-clamp data provided Hodgkin and Huxley with measurements of g_{Na} , τ_m and τ_h at each value of V_c . In addition, the best fit of Eq. 14.24 to the voltage-clamp data also indicated that $P = 3$ (see Eq. 14.20), which suggested that three gating particles regulated the activation gate of g_{Na}

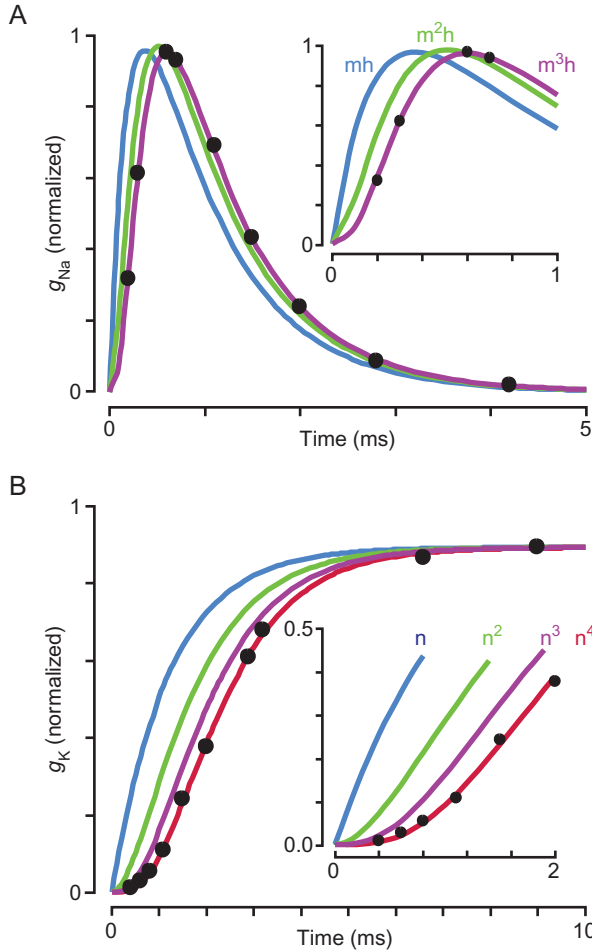


FIGURE 14.9 Estimating the number of gating particles that regulate each Na^+ and K^+ channel. The filled circles represent data from an experiment by Hodgkin and Huxley (axon 17). The inserts illustrate an enlargement of the first few milliseconds of the response. The ionic conductances, g_{Na} (A) and g_{K} (B), increase with a delay during a voltage-clamp step. This observation suggests that $P > 1$ in Eq. 14.20 (see also Fig. 14.8). To estimate appropriate values for P , empirical data are fit (solid lines) with equations similar to Eq. 14.20 (i.e., Eqs. 14.24 and 14.32) where the value for P is increased from 1 until an adequate fit of the data is achieved. The initial delay in g_{Na} is well fit with $P = 3$, while the corresponding value for g_{K} is $P = 4$. Adapted from Hodgkin and Huxley (1952d).

(see Fig. 14.8) and which produced a sigmoidal time course of $m(t)$ (see insert in Fig. 14.9). Thus, g_{Na} was described by:

$$g_{\text{Na}} = \bar{g}_{\text{Na}} m^3 h \quad (14.25)$$

where:

$$\begin{aligned} \frac{dm}{dt} &= \alpha_m(V_m)(1 - m) - \beta_m(V_m)m \\ \frac{dh}{dt} &= \alpha_h(V_m)(1 - h) - \beta_h(V_m)h \end{aligned} \quad (14.26a, b)$$

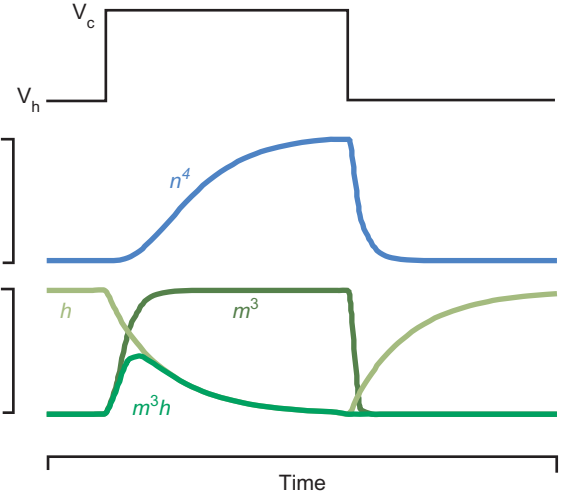


FIGURE 14.10 Temporal dynamics of n^4 , h , m^3 and m^3h during a hypothetical voltage-clamp step. Initially, the membrane potential is voltage clamped at a holding potential (V_h) near the resting potential (V_m). A command voltage (V_c) briefly steps the membrane potential to a depolarized level. During the voltage step, n and m are being activated, and thus, the curves for n^4 and m^3 followed the $(1 - \exp(-t/\tau))^P$ time course. Conversely, h is inactivated by depolarization, and thus, the curve for h follows the $\exp(-t/\tau)$ time course. In this schematic, the values for the time constants τ_m , τ_n and τ_h were adjusted to a ratio of 1:4:5, and the duration of the voltage-clamp step was the equivalent of $20 \times \tau_m$. The curves illustrate how n^4 and m^3h closely imitate the time courses of g_{Na} and g_{K} that are observed empirically (compare with Fig. 14.9).

or the equivalent expressions:

$$\frac{dm}{dt} = \frac{m_\infty(V_m) - m}{\tau_m(V_m)} \quad \frac{dh}{dt} = \frac{h_\infty(V_m) - h}{\tau_h(V_m)} \quad (14.27a, b)$$

where:

$$m_\infty(V_m) = \frac{\alpha_m(V_m)}{\alpha_m(V_m) + \beta_m(V_m)} \quad \tau_m(V_m) = \frac{1}{\alpha_m(V_m) + \beta_m(V_m)} \quad (14.28a, b)$$

$$h_\infty(V_m) = \frac{\alpha_h(V_m)}{\alpha_h(V_m) + \beta_h(V_m)} \quad \tau_h(V_m) = \frac{1}{\alpha_h(V_m) + \beta_h(V_m)} \quad (14.29a, b)$$

The time constants (i.e., $\tau_m(V_m)$ and $\tau_h(V_m)$) and the steady-state values of m and h (i.e., $m_\infty(V_m)$ and $h_\infty(V_m)$) were measured by fitting Eq. 14.24 to the voltage-clamp records of I_{Na} (Fig. 14.11A) and from these data the rate constants (i.e., $\alpha_m(V_m)$, $\beta_m(V_m)$, $\alpha_h(V_m)$, and $\beta_h(V_m)$) were calculated using Eqs. 14.22 and 14.23. The values for the rate constants were plotted as functions of voltage, and expressions for the voltage dependency of the rate constants were derived.

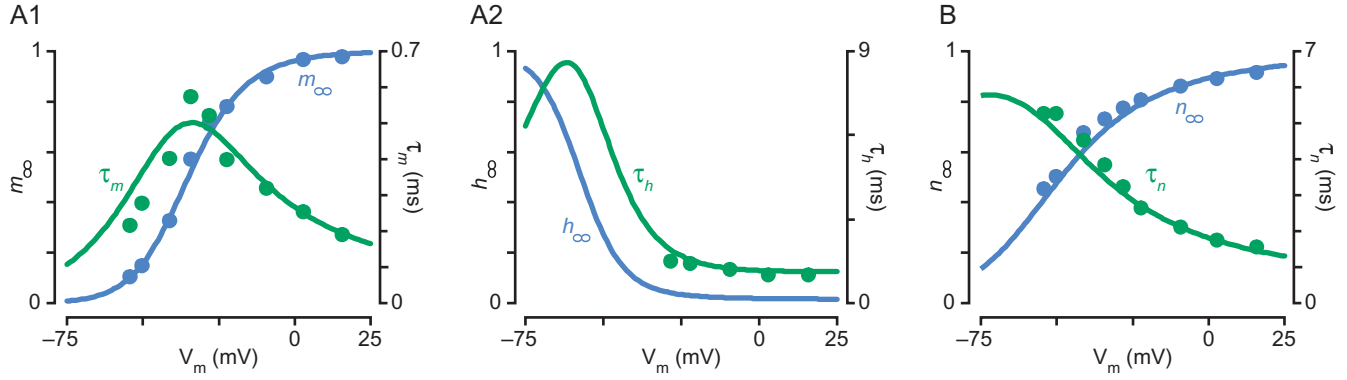


FIGURE 14.11 Voltage-dependences of gating variables and their respective time constants. The time constants (τ_m , τ_h and τ_n) and the steady-state activation (m_∞ and n_∞) and inactivation (h_∞) gating variables are plotted as functions of membrane potential (V_m) for the squid giant axon at 6.3° C. The filled circles represent data from an experiment by Hodgkin and Huxley (axon 17). The smooth curves were calculated using Eqs. 14.28 (Panel A1), 14.29 (Panel A2) and 14.36 (Panel B). **A1:** activation gating variable (m_∞) and its time constant (τ_m) for Na^+ conductance. **A2:** inactivation gating variable (h_∞) and its time constant (τ_h) for Na^+ conductance. **B:** activation gating variable (n_∞) and its time constant (τ_n) for K^+ conductance. The steady-state inactivation h_∞ is a monotonically decreasing function of voltage, whereas the steady-state activation variables m_∞ and n_∞ increase with membrane depolarization. Note that in Eqs. 14.25 and 14.33, the activation gating variables for Na^+ (i.e., m) and K^+ (i.e., n) are raised to the third and fourth powers, respectively. Thus, the functional voltage-dependent activation of I_{Na} and I_{K} is much steeper than represented in this illustration. Adapted from Hodgkin and Huxley (1952d).

Empirically, Hodgkin and Huxley derived the following equations for the rate constants:

$$\alpha_m(V_m) = \frac{0.1(V_r - V_m + 25)}{\exp\left(\frac{V_r - V_m + 25}{10}\right) - 1} \quad \beta_m(V_m) = 4 \exp\left(\frac{V_r - V_m}{18}\right) \quad (14.30a, b)$$

$$\alpha_h(V_m) = 0.07 \exp\left(\frac{V_r - V_m}{20}\right) \quad \beta_h(V_m) = \frac{1}{\exp\left(\frac{V_r - V_m + 30}{10}\right) + 1} \quad (14.31a, b)$$

where V_r is the resting potential (which is usually taken to be either -60 or -65 mV), V_m is the membrane potential in units of mV, and the rate constants (i.e., α_i and β_i) are expressed in units of ms^{-1} . (It should be noted that the conventions used by Hodgkin and Huxley to describe voltage were different from those in use today. Box 14.1 explains this difference.)

Although not indicated in Eqs. 14.26 and 14.27, the kinetics of the ionic conductances are influenced by temperature. Hodgkin and Huxley performed most of their voltage-clamp experiments with the preparations cooled to $\sim 6^\circ\text{C}$. The cooler temperature slowed the kinetics of the membrane currents, which in turn, made them easier to record and analyze. The standard parameters of the HH equations reflect a temperature of 6.3°C . The kinetics of the HH equations can be adjusted to reflect some other temperature (T) by multiplying the kinetic equations by a temperature coefficient $\Phi = Q_{10}^{\Delta T/10}$ (see the following) (FitzHugh, 1966; Hodgkin and Huxley, 1952d).

Characterizing the K^+ Conductance

Unlike I_{Na} , I_{K} did not inactivate during voltage-clamp steps (e.g., Fig. 14.3B2). Thus, Hodgkin and Huxley postulated that g_{K} was governed by a single type of gate, which governed the activation of g_{K} and which they termed n . To determine values for g_{K} , τ_n and p , the time course of g_{K} during voltage-clamps to various membrane potential was best described by:

$$g_{\text{K}}(t) = \left(g_{\infty}^{1/4}(V_c) - \left(g_{\infty}^{1/4}(V_c) - g_0^{1/4}\right) \exp^{-t/\tau_n(V_c)}\right)^4 \quad (14.32)$$

which indicated that four particles regulated the activation gate of g_{K} (Fig. 14.9B). The fourth power produces a sigmoidal time course of $n(t)$ (Fig. 14.10). Thus, g_{K} was described by:

$$g_{\text{K}} = \bar{g}_{\text{K}} n^4 \quad (14.33)$$

where:

$$\frac{dn}{dt} = \alpha_n(V_m)(1 - n) - \beta_n(V_m)n \quad (14.34)$$

or the equivalent expression:

$$\frac{dn}{dt} = \frac{n_{\infty}(V_m) - n}{\tau_n(V_m)} \quad (14.35)$$

where:

$$n_{\infty}(V_m) = \frac{\alpha_n(V_m)}{\alpha_n(V_m) + \beta_n(V_m)} \quad \tau_n(V_m) = \frac{1}{\alpha_n(V_m) + \beta_n(V_m)} \quad (14.36a, b)$$

BOX 14.1

UPDATING THE PARAMETERS IN THE HODGKIN-HUXLEY EQUATIONS

Although the original papers of [Hodgkin et al., 1952](#); [Hodgkin and Huxley, 1952a–d](#) were published over 60 years ago, this series of papers remains influential to the present day. The papers have been reprinted on several occasions ([Cooke and Lipkin, 1972](#); [Hodgkin and Huxley, 1990](#); [Moore and Stuart, 2000](#)), and the detailed descriptions of what have become known as the HH equations ([Cole et al., 1955](#)) are often included in modern textbooks about cellular neurophysiology and computational neuroscience ([Bower and Beeman, 1998](#); [Byrne and Schultz, 1994](#); [Cronin, 1987](#); [Dayan and Abbott, 2001](#); [DeSchutter, 2001](#); [Hille, 2001](#); [Johnston and Wu, 1997](#); [Koch, 1999](#); [MacGregor, 1987](#); [Tuckwell, 1988](#); [Ventriglia, 1994](#); [Weiss, 1997](#)). Although these modern descriptions of the HH equations are similar to those in the original publications, the present day values for the parameters often do not appear to agree with those used by Hodgkin and Huxley in 1952.

This apparent discrepancy arises from the conventions used by Hodgkin and Huxley to represent voltage. In their original series of papers, [Hodgkin et al. \(1952\)](#) choose to regard the resting potential as a positive quantity and the action potential as a negative (i.e., downward) deflection. In addition, the variable V (voltage) in the HH equations denoted the *displacement* of the membrane potential from its resting value. Thus, Hodgkin and Huxley defined V as $V = E - E_r$; where E was the absolute value of the membrane potential and E_r was the absolute value of the resting potential. With their

choice of conventions, depolarizations of the membrane potential were negative values (downward deflections) and inward membrane currents had a positive sign (upward deflections). For additional explanation of the conventions used by Hodgkin and Huxley, see [Rinzel \(1998\)](#).

This aspect of the papers by Hodgkin and Huxley conflicts with the current practices in which the intracellular electrode measures the membrane potential with respect to an external ground (i.e., the resting potential is a negative quantity), action potentials and depolarizations are positive (upward) deflections, inward membrane currents have a negative sign (downward deflections), and the voltage variable (V_m) in modern representations of the HH equations denotes the absolute membrane potential. The HH equations can be recast into modern conventions for polarity and using absolute membrane potential by simple subtraction and multiplication ([Palti, 1971a,b](#)). In the present chapter, the HH equations for a spaced-clamped patch of membrane, as well as the data that are plotted in the figures, were expressed using the modern conventions where V_m is the absolute membrane potential and V_r is the absolute value for the resting potential, which was usually taken to be -60 mV. At a conceptual level, the choice of conventions for membrane currents and voltage is inconsequential. It does matter a great deal, however, when one wishes to implement and simulate the HH model.

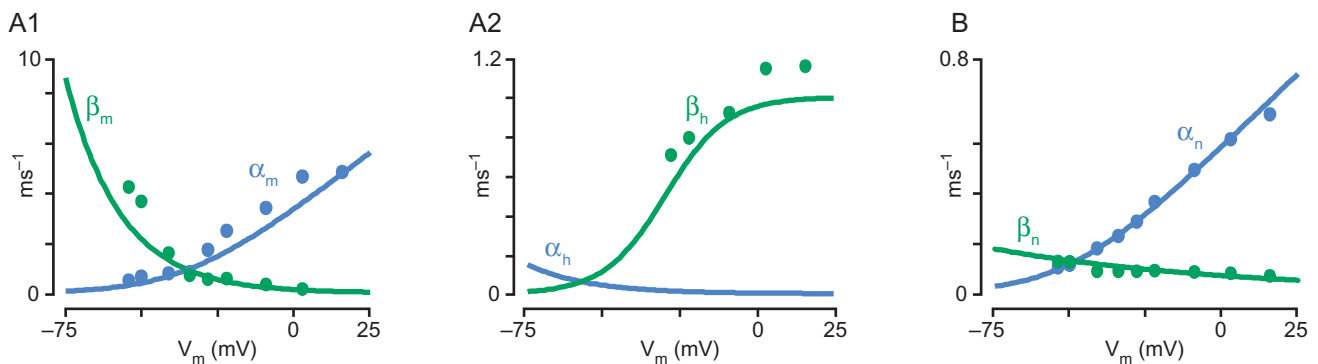


FIGURE 14.12 Voltage-dependences of the rate coefficients for the HH model of a squid giant axon at 6.3°C . The filled circles represent data from an experiment by Hodgkin and Huxley (axon 17). The smooth curves were calculated from Eqs. 14.30 (Panel A1), 14.31 (Panel A2) and 14.37 (Panel B). **A1:** forward (α_m) and backward (β_m) rate coefficients for activation of the Na^+ conductance. **A2:** forward (α_h) and backward (β_h) rate coefficients for inactivation of the Na^+ conductance. **B:** forward (α_n) and backward (β_n) rate coefficients for activation of the K^+ conductance. The forward rate coefficients for activation of Na^+ and K^+ (α_m and α_n , respectively) increase with membrane depolarization because m and n gating particles move into a permissive state in response to membrane depolarization (see [Fig. 14.6](#)). Conversely, the forward rate coefficient for inactivation of Na^+ (α_h) decreases with membrane depolarization because the h gating particle moves into a nonpermissive state in response to membrane depolarization. Adapted from [Hodgkin and Huxley \(1952d\)](#).

The time constant (i.e., $\tau_n(V_m)$) and steady values of n (i.e., $n_\infty(V_m)$) were measured (Fig. 14.11B) and from these data the rate constants (i.e., $\alpha_n(V_m)$ and $\beta_n(V_m)$) were calculated (Fig. 14.12B). The empirically determined expressions for the voltage dependency of the rate constants are:

$$\begin{aligned}\alpha_n(V_m) &= \frac{0.01(V_r - V_m + 10)}{\exp\left(\frac{V_r - V_m + 10}{10}\right) - 1} \\ \beta_n(V_m) &= 0.125 \exp\left(\frac{V_r - V_m}{80}\right)\end{aligned}\quad (14.37a, b)$$

where V_r is the resting potential of the cell in units of mV, V_m is the membrane potential in units of mV and $\alpha_n(V_m)$ and $\beta_n(V_m)$ are given in units of ms^{-1} .

Simulations of the Hodgkin-Huxley Equations

By incorporating Eqs. 14.25 and 14.33 into Eq. 14.8, it is possible to write a single equation that describes the total membrane current (I_m):

$$\begin{aligned}I_m = C_m \frac{dV}{dt} + \bar{g}_{\text{Na}} m^3 h (V_m - E_{\text{Na}}) + \bar{g}_{\text{K}} n^4 (V_m - E_{\text{K}}) \\ + \bar{g}_{\text{I}} (V_m - E_{\text{I}})\end{aligned}\quad (14.38)$$

This nonlinear differential equation, in addition to the three linear differential equations that describe the temporal evolution of the rate constants (i.e., Eqs. 14.26a, b and 14.34) constitutes the four-dimensional Hodgkin and Huxley model for a space-clamped patch of membrane (i.e., Fig. 14.1). These equations and their associated algebraic functions and parameters were derived to mathematically describe the magnitude and time course of I_{Na} and I_{K} produced by a series of voltage-clamp step depolarizations. As a first step toward validating their model, Hodgkin and Huxley tested the ability of the model to correctly calculate the total membrane current during a series of voltage-clamp steps. At a constant voltage, $dV/dt = 0$ and the steady-state values of the rate constants (i.e., $\alpha(V_m)$ and $\beta(V_m)$) are constant. The solution is then obtained directly in terms of the expressions given for $m(V_m, t)$, $h(V_m, t)$, $n(V_m, t)$ (i.e., Eqs. 14.26a, b, and 14.34). Using only a mechanical desk calculator (see Box 14.2), Andrew Huxley computed I_m for a number of different voltages and compared these computations to similar empirical data. This comparison is illustrated in Fig. 14.13. There is excellent agreement between the calculated membrane currents and empirical voltage-clamp records, which lent credence to the model.

The overriding goal of Hodgkin and Huxley's quantitative analysis of voltage-clamp currents, however, was to explain neuronal excitability, and the ultimate

test of the model was to see if it could quantitatively describe the action potential. Thus, Hodgkin and Huxley concluded their studies with calculations of the membrane potential changes predicted by their equations. In the absence of the feedback amplifier (i.e., without the voltage clamp), dV/dt was no longer constant, and there is no explicit solution to Eq. 14.38. Using numerical methods, Hodgkin and Huxley solved the equations and computed an action potential waveform that duplicated with remarkable accuracy the naturally occurring action potential (Fig. 14.14). In addition to describing the space-clamped action potential, Hodgkin and Huxley demonstrated the considerable power of their model to predict many other properties of neuronal excitability, including subthreshold responses, a sharp threshold for firing, membrane conductance changes during an action potential, the effects of temperature on the action potential waveform, propagated action potentials, ionic fluxes, absolute and relative refractory periods, anode break excitation and accommodation. Although the model has some limitations (see Box 14.3), the remarkable success of the HH model to accurately describe such a wide array of phenomena remains to this day a triumph of classical biophysics in understanding a fundamental neuronal property (i.e., excitability).

One of the great advantages of having a mathematical model of a complex process (e.g., neuronal excitability) is that it provides an opportunity to examine the component processes in ways that may not be experimentally possible. For example, it is possible to calculate the time courses and magnitudes of the different ionic currents, conductances and gating variables during an action potential (see Chapter 12). Similarly, it is possible to calculate the individual ionic currents during voltage-clamp steps (Fig. 14.15). Given that the tools (i.e., computers and software) necessary to simulate the HH model are readily available (see Box 14.2), anyone who wishes to explore the rich dynamical properties of these equations can easily do so.

Summary

The HH model describes neuronal excitability in terms of four variables: the membrane potential, $V_m(t)$, and three gating variables, $m(V, t)$, $h(V, t)$, and $n(V, t)$, which describe the permeability (i.e., conductance) of the membrane to Na^+ and K^+ (i.e., g_{Na} and g_{K}). The magnitude of the activation gating variables (i.e., $m(V, t)$ and $n(V, t)$) increases with increasing depolarization, whereas the magnitude of the inactivation gating variable (i.e., $h(V, t)$) decreases with depolarization. The gating variables were described by first-order differential equations with two voltage-dependent terms: the

BOX 14.2

COMPUTING SOLUTIONS TO THE HODGKIN-HUXLEY EQUATIONS

Hodgkin and Huxley conducted their voltage-clamp experiments on the squid giant axon at the Marine Biological Laboratory in Plymouth, England. Although the Plymouth laboratory was badly damaged during the great air raids of 1941, it was partially rebuilt by the time Hodgkin and Huxley arrived in July of 1949. With the help of Bernard Katz and their improved voltage-clamp apparatus, it took them only a month to obtain all of the voltage-clamp records that were used in the five papers published in 1952 (Hodgkin et al., 1952; Hodgkin and Huxley, 1952a–d). Upon returning to the University of Cambridge, they spent the next two years analyzing the data and preparing the manuscripts. By March 1951, they had settled on a set of the equations and parameters that adequately described the time course, magnitude and voltage dependency of the membrane currents that were observed during voltage-clamp steps. It was by no means a foregone conclusion, however, that these same equations would describe the behavior of the membrane under its normal operating conditions. Thus, the final stage of their analysis was to calculate the response of their mathematical representation of the nerve to the equivalent of an electrical stimulus. If the calculations produced an action potential that agreed favorably with experimental data, this would help validate their model.

Hodgkin and Huxley planned to solve their equations on the first electronic computer at the University of Cambridge, the EDSAC (electronic delay storage automatic calculator). Construction of the EDSAC was completed in 1949, and at that time, it was the state-of-the-art for electronic digital computing (Wheeler, 1992a,b). EDSAC was approximately 12 feet by 12 feet in size, had a power consumption of 12 kW, contained some 3000 vacuum tubes and had about 2000 bytes of nonrandom access memory, which was constructed from a series of five-foot-long tubes filled with mercury. EDSAC operated at 500 kHz and could perform 650 instructions per second. Division of two numbers took the EDSAC about 200 msec. Unfortunately for Hodgkin and Huxley, the EDSAC was undergoing major modifications in March of 1951 and would be unavailable for 6 months.

Hodgkin and Huxley overcame this setback by solving the differential equations numerically with a mechanical Brunsviga desk calculator (Schwiening, 2012). This was a laborious task. A space-clamped action potential (e.g., Fig. 14.14A) took a matter of days to compute, and a propagated action potential (e.g., Fig. 15 of Hodgkin and Huxley (1952d)) took a matter of weeks. In

addition to the space-clamped and propagated action potentials, Hodgkin and Huxley's computations included the impedance changes and the total movements of Na^+ and K^+ ions into and out of the axon during an action potential; recovery during the relative refractory period; anode break excitation; and the oscillatory response of the membrane to a rectangular pulse of current. These results were published in 1952 (Hodgkin and Huxley, 1952d) and showed surprisingly good agreement with the available empirical data from the giant axon. This agreement suggested that the formulations developed by Hodgkin and Huxley were substantially correct.

The scope of Hodgkin and Huxley's computations was limited, however, by the fact that an automatic computer was unavailable. The manual methods of solving the HH equations were so laborious as to discourage more detailed and broader investigations of the ability of the HH equations to predict and interpret the well-established and fundamental characteristics of nerve behavior. For example, the all-or-none nature of initiating an action potential was considered to be a key feature of neuronal excitability, but it was unknown whether the HH equations manifested this key feature.

To address these issues, Kenneth Cole and his colleagues (1955) wrote the machine language program necessary to run simulations of the HH equations on the first fully operational stored-program electronic computer in the United States, the SEAC (standards eastern automatic computer). Construction of the SEAC was completed in 1950. Its design and capabilities were comparable to the EDSAC (Kirsch, 1998). Although it was not their goal to cross check the original calculations of Hodgkin and Huxley, the first computer simulation of the HH equations by Cole et al. in 1955 was of a space-clamped action potential (see Fig. 1 of Cole et al. (1955)). The results from Huxley's hand calculations and from the computer simulation were indistinguishable. Moreover, the SEAC calculations provided evidence the HH equations manifest an all-or-none response to current stimulation. Although some (including Huxley (1959)) doubted the threshold phenomena observed by Cole et al., the independent replication of the action potential calculation served to increase confidence in the HH equations.

In theory, using a computer should increase the speed and accuracy of solving the HH equations. In practice, however, this was not always the case in the early days of computers. Although, SEAC could

BOX 14.2 (cont'd)

calculate the space-clamped action potential in about 30 min, accessing the computer proved very slow (FitzHugh, 1960). Solutions took a week or more, including the time for relaying instructions to the programming and operating technicians, scheduling time on the computer, and receiving the results. In addition, a flaw was detected in the machine language program for the first computer simulation of the HH equations (FitzHugh and Antosiewicz, 1959). The program contained division by zero errors in the calculations of α_m and α_n . The major effect of these errors was to produce a spurious saddle point (see Box 14.4). It was an unfortunate accident that the spurious saddle point appeared near the membrane potential at which the threshold was believed to occur. In 1959, FitzHugh and Antosiewicz (1959) reprogrammed the HH equations in FORTRAN, avoiding the division by zero errors, and, using an IBM 704, reexamined the issue of all-or-none responses in the HH equations. On recalculation, the all-or-none threshold was lost, and the HH equations were found to manifest a “quasi-threshold” phenomenon (FitzHugh and Antosiewicz, 1959): i.e., over a sufficiently small range of stimulus intensities the amplitude of the action potential decreases continuously from an “all” to a “none” (see Fig. 2 of FitzHugh and Antosiewicz (1959)). The sharpness of threshold phenomenon is determined by the steepness of the stimulus-response curve for the peak amplitude versus stimulus intensity. The HH equations manifest a very sharp threshold. An increase in the stimulus intensity of only one part in 10^8 was sufficient to

distinguish between a very small graded response and a complete action potential. Thus, the lack of a mathematically correct threshold (i.e., saddle point) seemed entirely academic, and faith in the HH equations was not shaken. Indeed, the computational prediction of quasi-threshold behavior was subsequently confirmed with experimental studies (Cole et al., 1970), which further increased confidence in the HH equations.

At present, access to computers is no longer a limiting factor to individuals who wish to simulate the HH model. Commonly available personal computers are more than adequate to calculate solutions to the HH equations. In addition, simulating the HH model is no longer limited to individuals with skills necessary to develop the computer programs required to solve the HH equations. It is possible to solve the HH equations using commonly available spreadsheet programs (Brown, 1999, 2000) and there are many freely available and user-friendly software packages that have been developed to simulate HH type models of neurons. Software packages that are specifically designed to build and simulate models of HH type neurons and neural circuits are commonly referred to as *neurosimulators*. Some examples of neurosimulators include GENESIS (Bower and Beeman, 1998), NEURON (Hines and Carnevale, 1997) and SNNAP (Baxter and Byrne, 2007; Ziv et al., 1994). There are several reviews that describe the features and availability of neurosimulators (Brette et al., 2007; DeSchutter, 1989, 1992; Hayes et al., 2002).

steady-state activation or inactivation (i.e., $m(V_m)$, $h_\infty(V_m)$, $n_\infty(V_m)$) and the time constant ($\tau_m(V_m)$, $\tau_h(V_m)$, $\tau_n(V_m)$). Thus, the HH model (Hodgkin and Huxley 1952d) for a spaced-clamped patch of membrane (i.e., an isopotential compartment) is a system of four ordinary differential equations:

$$I_m = C_m \frac{dV}{dt} + \bar{g}_{\text{Na}} m^3 h (V_m - E_{\text{Na}}) + \bar{g}_K n^4 (V_m - E_K) + \bar{g}_l (V_m - E_l) \quad (14.39)$$

$$\frac{dm}{dt} = \Phi(T) \frac{m_\infty(V_m) - m}{\tau_m(V_m)} = \Phi(T) [\alpha_m(V_m)(1 - m) - \beta_m(V_m)m] \quad (14.40)$$

$$\frac{dh}{dt} = \Phi(T) \frac{h_\infty(V_m) - h}{\tau_h(V_m)} = \Phi(T) [\alpha_h(V_m)(1 - h) - \beta_h(V_m)h] \quad (14.41)$$

$$\frac{dn}{dt} = \Phi(T) \frac{n_\infty(V_m) - n}{\tau_n(V_m)} = \Phi(T) [\alpha_n(V_m)(1 - n) - \beta_n(V_m)n] \quad (14.42)$$

where the coefficient $\Phi(T)$ describes the effects of temperature on the three gating variables (see below) and the voltage- and time-dependency of the gating variables are given by:

$$m_\infty(V_m) = \frac{\alpha_m(V_m)}{\alpha_m(V_m) + \beta_m(V_m)}, \quad \tau_m(V_m) = \frac{1}{\alpha_m(V_m) + \beta_m(V_m)} \quad (14.43a, b)$$

$$h_\infty(V_m) = \frac{\alpha_h(V_m)}{\alpha_h(V_m) + \beta_h(V_m)}, \quad \tau_h(V) = \frac{1}{\alpha_h(V_m) + \beta_h(V_m)} \quad (14.44a, b)$$

$$n_\infty(V_m) = \frac{\alpha_n(V_m)}{\alpha_n(V_m) + \beta_n(V_m)}, \quad \tau_n(V_m) = \frac{1}{\alpha_n(V_m) + \beta_n(V_m)} \quad (14.45a, b)$$

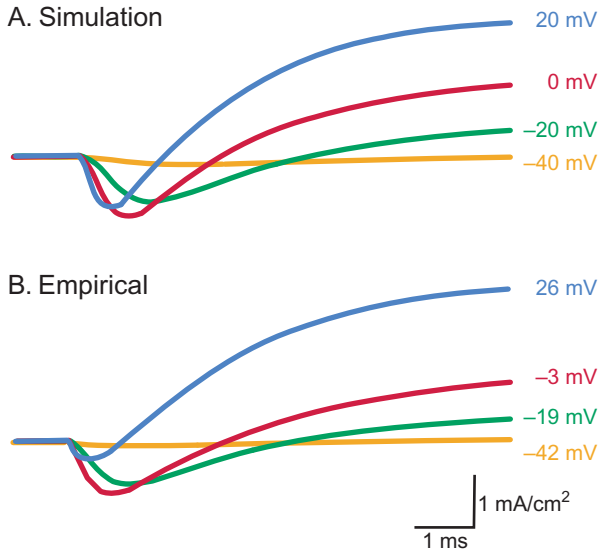


FIGURE 14.13 Comparison of simulated membrane current and empirical observations. **A:** As a first test of their model, Hodgkin and Huxley used Eq. 14.38 to compute the membrane current that would be elicited by a series of voltage-clamp steps. Four of the calculated traces are illustrated. They represent the predicted total membrane current during voltage-clamp steps to -40 , -20 , 0 and 20 mV. **B:** Empirical data from one of Hodgkin and Huxley's voltage-clamp experiments (axon 31 at 4°C). The empirical data were collected from a series of voltage-clamp steps to -42 , -19 , -3 and 26 mV. There was excellent agreement between the simulated and empirical data, which suggests that the HH equations captured the salient features of the experimental data. Adapted from Hodgkin and Huxley (1952d).

These equations relate the membrane potential (i.e., V_m) to the permeability of the membrane to Na^+ , K^+ and the nonspecific leakage of ions. The equations contain several auxiliary parameters representing equilibrium potentials of the ions (i.e., E_{Na} , E_{K} and E_l); maximum ionic conductances (i.e., \bar{g}_{Na} , \bar{g}_{K} and \bar{g}_l), temperature coefficient (i.e., Φ), and the capacitance of the membrane (i.e., C_m). Values for these parameters were obtained from analyses of experimental data (Hodgkin et al., 1952; Hodgkin and Huxley, 1952a–c). The values used by Hodgkin and Huxley (1952d) to describe the squid giant axon were:

$$\begin{aligned} E_{\text{Na}} &= V_r + 115 \text{ mV} & \bar{g}_{\text{Na}} &= 120 \text{ mS/cm}^2 \\ E_{\text{K}} &= V_r - 12 \text{ mV} & \bar{g}_{\text{K}} &= 36 \text{ mS/cm}^2 \\ E_l &= V_r + 10.613 \text{ mV} & \bar{g}_l &= 0.3 \text{ mS/cm}^2 \\ \Phi(T) &= 3^{(T-6.3)/10} & C_m &= 1 \mu\text{F/cm}^2 \end{aligned}$$

where V_r is resting membrane potential of the cell, T is temperature in degrees centigrade. The coefficient Φ provides the three gating variables with a Q_{10} of 3, and equals 1 at Hodgkin and Huxley's standard temperature of 6.3°C . The rate constants (i.e., α_i and β_i) were estimated by fitting empirically derived exponential

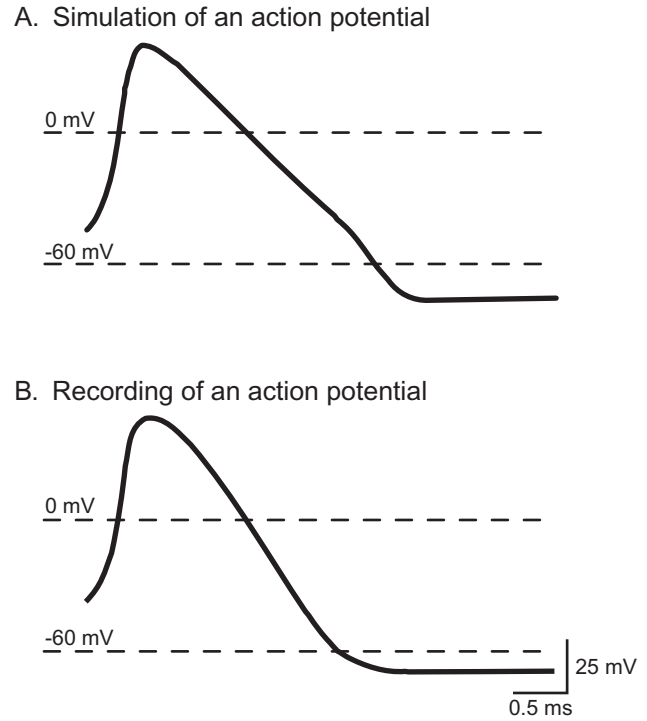


FIGURE 14.14 Comparison of simulated space-clamped action potential and empirical observations. If a giant axon is stimulated simultaneously over a substantial portion of its length (e.g., by applying a shock to a long internal electrode), all points within that length will undergo an action potential simultaneously (see Chapter 12). There will be no difference of potential along the axis of the nerve fiber, and therefore no longitudinal current. This type of action potential is referred to as a “space-clamped” (as opposed to a propagated) action potential. **A:** Simulation of a space-clamped action potential. The solution of Eq. 14.38 describes the membrane potential of a space-clamped patch of membrane. If the equivalent of a suprathreshold electrical shock is incorporated in Eq. 14.38, an action potential is produced. This example was produced by Hodgkin and Huxley, who used a mechanical desk calculator to solve the set of differential equations that have come to be known as the HH equations (Eqs. 14.39–14.42). **B:** An action potential recorded under experimental conditions that matched those simulated in Panel A (i.e., spaced-clamp patch of membrane, temperature of 6°C). There is good agreement between the theoretical and empirical action potentials. This agreement suggests that the formulations developed by Hodgkin and Huxley accurately represented the processes that underlie the action potential. Adapted from Hodgkin and Huxley (1952d).

functions of voltage to the experimental data. For the squid giant axon at a temperature of 6.3°C , these functions were (Hodgkin and Huxley, 1952d):

$$\alpha_m(V_m) = \frac{0.1(V_r - V_m + 25)}{\exp\left(\frac{V_r - V_m + 25}{10}\right) - 1} \quad \beta_m(V_m) = 4 \exp\left(\frac{V_r - V_m}{18}\right) \quad (14.46a, b)$$

$$\alpha_h(V_m) = 0.07 \exp\left(\frac{V_r - V_m}{20}\right) \quad \beta_h(V_m) = \frac{1}{\exp\left(\frac{V_r - V_m + 30}{10}\right) + 1} \quad (14.47a, b)$$

BOX 14.3

LIMITATIONS OF THE HODGKIN-HUXLEY EQUATIONS

The HH model has been so widely accepted as a paradigm for excitable membranes that its appropriateness for the squid giant axon itself has generally not been questioned. The model fails, however, to provide a good description for some electrophysiological properties of the axon. For example, in response to a relatively long-duration, suprathreshold current pulse, the axon generally produces a single action potential (i.e., accommodation). In contrast, the HH model predicts sustained spiking activity throughout the stimulus (Clay, 1998; Clay et al., 2008). This discrepancy can be attributed to the assumption by Hodgkin and Huxley that the activation (m) and inactivation (h) of the Na^+ conductance were independent processes, whereas empirical evidence indicates the two processes are coupled (Bezanilla and Armstrong, 1977). A revised version of the HH model (Clay, 1998; Vandenberg and Bezanilla, 1991), which incorporates coupling between activation and inactivation, provides a better description of the squid axon (for alternative solutions, see Clay et al., 2008).

Other assumptions inherent in the HH model have been examined and found to be only approximately valid. In the model, temperature is assumed to affect only the kinetics of the ionic conductances (see Eqs. 14.40–14.42). The conductance of an ionic channel is also altered by temperature, albeit to a relatively small degree (Hille, 2001). If the HH equations are modified to incorporate an effect of temperature on the conductances, a better fit of empirical data is achieved (FitzHugh, 1966). Another assumption within the model is that the flow of ionic current through open channels obeys Ohm's law. Current data, however, suggest that the linearity is only approximate and holds neither under all ionic conditions nor in Na^+ and K^+ channels

of all organisms (Hille, 2001). For example, Na^+ channels are not ohmic in nodes of Ranvier (Dodge and Frankenhaeuser, 1959).

Rather than detracting from the HH model, these experimental results highlight some of the advantages of formulating a detailed, quantitative model. First, the formulation of the model forces one to clearly and quantitatively state the assumptions that underlie the model and to evaluate the impact of these assumptions on the behavior of the model. This procedure, in turn, provides guidelines for future experimental studies that can directly test the enumerated assumptions. Second, the model provides a modifiable framework with which new data and concepts can be incorporated and evaluated. Hodgkin and Huxley were well aware that their model had limitations. In their discussion of the model (Hodgkin and Huxley, 1952d), they acknowledged the shortcomings of the model and pointed out some discrepancies between the calculated and observed behavior of the squid giant axon. For example, the waveform of the calculated action potential had sharper peak and small "hump" in the falling phase that was not present in the recorded action potential (closely compare the two action potentials in Fig. 14.14). As Huxley stated in 1964, "I would not like to leave you with the impression that the particular equations we produced in 1952 are definitive. ... Hodgkin and I feel that these equations should be regarded as a first approximation which needs to be refined and extended in many ways in the search for the actual mechanisms of the permeability changes on the molecular scale." Even if its details cannot be taken literally, the HH model continues to have important general properties with mechanistic implications that are helping to direct future studies, both empirical and computational.

$$\alpha_n(V_m) = \frac{0.01(V_r - V_m + 10)}{\exp\left(\frac{V_r - V_m + 10}{10}\right) - 1} \quad \beta_n(V_m) = 0.125 \exp\left(\frac{V_r - V_m}{80}\right) \quad (14.48a,b)$$

The work of Hodgkin and Huxley was a landmark in the field of biophysical research. Their protocol involved voltage-clamp analysis of membrane currents, separating the membrane current into its components, developing and fitting kinetic schemes for the time- and voltage-dependences of the ionic conductances, and finally, reconstructing the action potential. This work established a precedent for combining experimental and computational techniques to explore

excitable membrane systems. This interdisciplinary approach is still commonly used, and Hodgkin-Huxley formalisms remain a cornerstone of quantitative models of neuronal excitability.

A GEOMETRIC ANALYSIS OF EXCITABILITY

The HH equations constitute a remarkably successful quantitative model. With reasonable accuracy, the model describes the membrane currents and the action potential of squid giant axon, as well as a number of

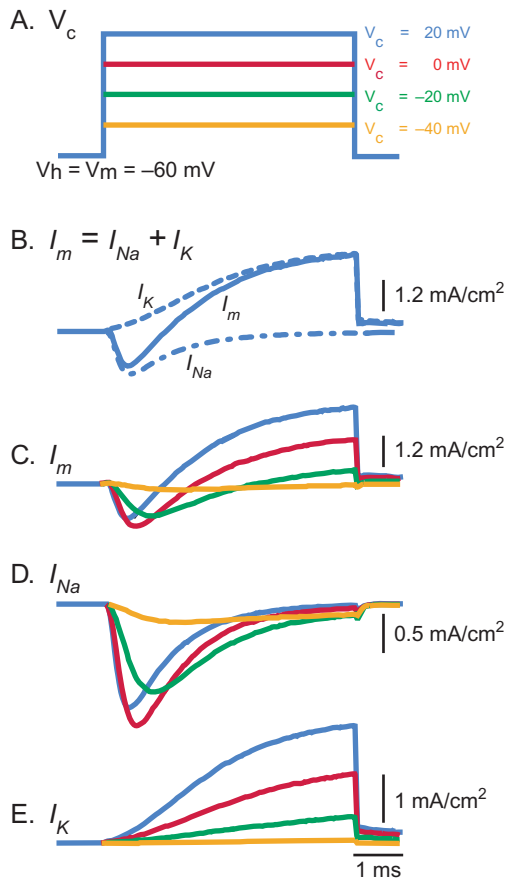


FIGURE 14.15 Simulation of a voltage-clamp experiment.

Solving the HH equations is much easier today than it was for Hodgkin and Huxley in 1952 (see [Box 14.2](#)). Digital computers are widely available and there are many software packages available that have been designed to simulate neuronal properties. Such simulations can provide a useful tool for gaining insights into the complex and nonlinear processes that underlie neuronal excitability. **A:** In these simulations, which were produced using the simulation package SNNAP ([Baxter and Byrne 2007](#); [Ziv et al., 1994](#)), the holding potential (V_h) was equal to the resting membrane potential (V_m), which was taken to be -60 mV. The command voltage (V_c) briefly steps the membrane potential to various depolarized values. The values of V_c are indicated next to each trace. The colors of each voltage-clamp step in Panel A correspond to the membrane currents in Panels B–E. **B:** The simulated membrane current (I_m) is composed primarily of I_{Na} and I_K . **C:** The total membrane current is computed by solving [Eq. 14.38](#). I_m has an early inward component that is followed by a large, sustained outward component. The overall appearance of these simulated membrane currents agrees well with empirical data (e.g., [Fig. 14.13B](#)) and with the original calculations of Hodgkin and Huxley (e.g., [Fig. 14.13A](#)). **D:** I_{Na} in isolation. Note that the largest I_{Na} trace (i.e., the red trace) does not occur during the largest voltage-clamp step (i.e., the blue trace). As V_c approaches E_{Na} , the driving force for I_{Na} approaches zero and the magnitude of the current decreases (see [Eq. 14.3](#)). **E:** I_K in isolation. Unlike I_{Na} , I_K increases monotonically as a function of increasing V_c . In addition, because the description of g_K (i.e., [Eq. 14.33](#)) has only an activation gating variable, I_K is sustained throughout the duration of the voltage-clamp step.

other dynamical properties of neuronal excitability, such as anode break excitation, accommodation, and the refractory period (see Chapter 12). Although this quantitative, conductance-based model has been enormously fruitful in terms of providing a mathematical framework for modeling neuronal excitability, it has a serious drawback, i.e., its numerical complexity. The HH equations are highly nonlinear (i.e., m is raised to the third power and n is raised to the fourth power) and complex (i.e., the model consists of four coupled differential equations, a large number of algebraic equations and a host of parameters). This complexity makes it difficult to intuitively understand the workings of the model. Indeed, Andrew Huxley may have said it best when he stated ([Huxley 1964](#)): “Very often my expectations turned out to be wrong, and an important lesson I learned from these manual computations was the complete inadequacy of one’s intuition in trying to deal with a system of this degree of complexity.”

To gain intuitive insight into the dynamical properties of neurons, it is helpful to examine less complex models that manifest the salient features of neuronal excitability. By exploiting a low-dimensional (i.e., two or three differential equations) model of an excitable membrane and by applying techniques from the mathematical field of nonlinear dynamics, many dynamical properties of neurons (e.g., threshold behavior, excitability, repetitive firing, autonomous bursting) can be understood, predicted and interpreted. Others have used this approach and have found that it is considerably easier—from a numerical and a conceptual point of view—to study the dynamical properties of neurons described by reduced models rather than simulating the behavior of biophysically complex neurons (see [Box 14.5](#); [Abbott, 1994](#); [Av-Ron et al., 1991](#); [Alexander and Cai, 1991](#); [Bertram, 1994](#); [Bertram et al., 1995](#); [Butera et al., 1996](#); [Butera, 1998](#); [Canavier et al., 2002](#); [Drion et al., 2012](#); [Ermentrout, 1996](#); [FitzHugh, 1960](#); [Gall and Zhou, 2000](#); [Hoppensteadt, 2013](#); [Hoppensteadt and Izhikevich, 2001](#); [Izhikevich, 2000, 2001, 2010](#); [Kepler et al., 1992](#); [Koch, 1999](#); [Qi et al., 2013](#); [Rinzel, 1985](#); [Rinzel and Ermentrout, 1998](#)) (see also Chapter 6). The second half of this chapter will illustrate how to develop reduced models of excitability and how to analyze their dynamical properties.

Two-Dimensional Reduction of the Hodgkin-Huxley Model

The HH model can be reduced to a two-variable model by identifying and combining variables with similar time scales and biophysical roles and by

allowing relatively fast variables to be instantaneous. For example, the time constant for m is an order of magnitude faster than those of h or n (Fig. 14.11). Thus, it is reasonable to approximate m by $m_\infty(V_m)$, which eliminates one of the differential equation (i.e., Eq. 14.26a). In addition, the variables n and h evolve on similar time scales and with an approximately constant relationship between their values (i.e., the sum of $n(V_m, t)$ and $-h(V_m, t)$ is approximately constant). Thus, it is reasonable to combine h and n into a single “recovery” variable, which has been termed w (FitzHugh, 1961; Rinzel, 1985). Using a single recovery variable replaces two of the differential equations (i.e., Eqs. 14.26b and 14.34) with a single expression for dw/dt (see below). By incorporating these approximations and some additional simplifications in the algebraic equations, it is possible to produce a tractable, two-variable model (i.e., a model with only dV_m/dt and dw/dt) that is versatile, that manifests many of the salient features of neuronal excitability, and that manifests a rich and diverse array of dynamical properties.

The reduced model (Av-Ron et al., 1991) includes a linear leakage current (I_l) and an externally applied stimulus current (I_s), as well as a time- and voltage-dependent inward current (I_{Na}) and outward current (I_K). The inward current is rapidly activated by depolarization, and contributes to its own further activation by producing further depolarization (i.e., autocatalytic or positive feedback). This positive feedback process has an instantaneous dependence on membrane potential. There is also a slower, negative feedback process. With depolarization, w increases, leading to activation of I_K and inactivation of I_{Na} . The dynamics of this two-dimensional system are described by the following differential equations:

$$\frac{dV_m}{dt} = \frac{-(I_{Na} + I_K + I_l - I_s)}{C_m} \quad (14.49)$$

$$\frac{dw}{dt} = \Phi(T) \frac{w_\infty(V_m) - w}{\tau_w(V_m)} \quad (14.50)$$

where V_m is the absolute membrane potential, C_m is the membrane capacitance, and $\Phi(T)$ is similar to the temperature coefficient in the HH equations. The currents are described by:

$$I_{Na} = \bar{g}_{Na} m_\infty^{mp}(V_m)(1 - w(V_m, t))(V_m - E_{Na}) \quad (14.51)$$

$$I_K = \bar{g}_K \left(\frac{w(V_m, t)}{s} \right)^{wp} (V_m - E_K) \quad (14.52)$$

$$I_l = \bar{g}_l (V_m - E_l) \quad (14.53)$$

where \bar{g}_i represents the maximum conductances of a given ionic current, E_i represents the equilibrium

potential for a given ionic current, mp and wp are parameters and s is a scaling factor that allows the magnitude of recovery variable (i.e., w) to be different for I_{Na} and I_K . The following equations give the voltage dependencies of the steady-state of the recovery variable (i.e., w_∞), the steady-state of the Na^+ activation variable (i.e., m_∞), and the relaxation function of the recovery variable (i.e. τ_w):

$$w_\infty(V_m) = \frac{1}{1 + \exp(-2a^{(w)}(V_m - V_{1/2}^{(w)}))} \quad (14.54)$$

$$m_\infty(V_m) = \frac{1}{1 + \exp(-2a^{(m)}(V_m - V_{1/2}^{(m)}))} \quad (14.55)$$

$$\tau_w(V_m) = \frac{1}{\bar{\lambda} + \exp(a^{(w)}(V_m - V_{1/2}^{(w)})) + \bar{\lambda} \exp(-a^{(w)}(V_m - V_{1/2}^{(w)}))} \quad (14.56)$$

where Eqs. 14.54 and 14.55 are sigmoid curves and $V_{1/2}^{(w)}$ is the voltage for the half maximal value and parameter $a^{(w)}$ controls the slope of the curve at this midpoint (i.e., inflection point). Eq. 14.56 is a bimodal sigmoid and the parameter $\bar{\lambda}$ represents the effects of $\Phi(T)$ in Eq. 14.40. For additional details of this reduced model, see Av-Ron et al. (1991).

This reduced model (Eqs. 14.49 and 14.50) can exhibit two major types of qualitative behavior. For some parameter regimes, the model is normally quiescent, but excitable in that it can fire one or more action potentials in response to transient stimuli (Fig. 14.16A). For different parameter regimes, the model fires action potentials in a repetitive fashion (i.e., limit cycle oscillations) (Fig. 14.17B). In addition, for some parameter regimes, the model can manifest at least one type of bistability (Fig. 14.19B), which underlies some types of burst firing. The same nonlinear properties that allow the model to fire a single action potential also enable it to function as a nonlinear oscillator, generating sustained rhythmic activity. How can such distinct behaviors emerge from such a simple system, and how can the behavior of the system be predicted? With parameter variations, a series of examples can be generated in a way that explains how the nonlinear properties of this simple two-dimensional model endow the system with such rich dynamical behaviors. Several methods (e.g., phase planes, nullclines, stability and bifurcations) also can be used to develop an intuitive understanding of the workings of this model (see Box 14.4). This approach closely follows that used by Rinzel and Ermentrout (1998) to analyze a different model (i.e., the Morris-Lecar model) and has been used by Av-Ron

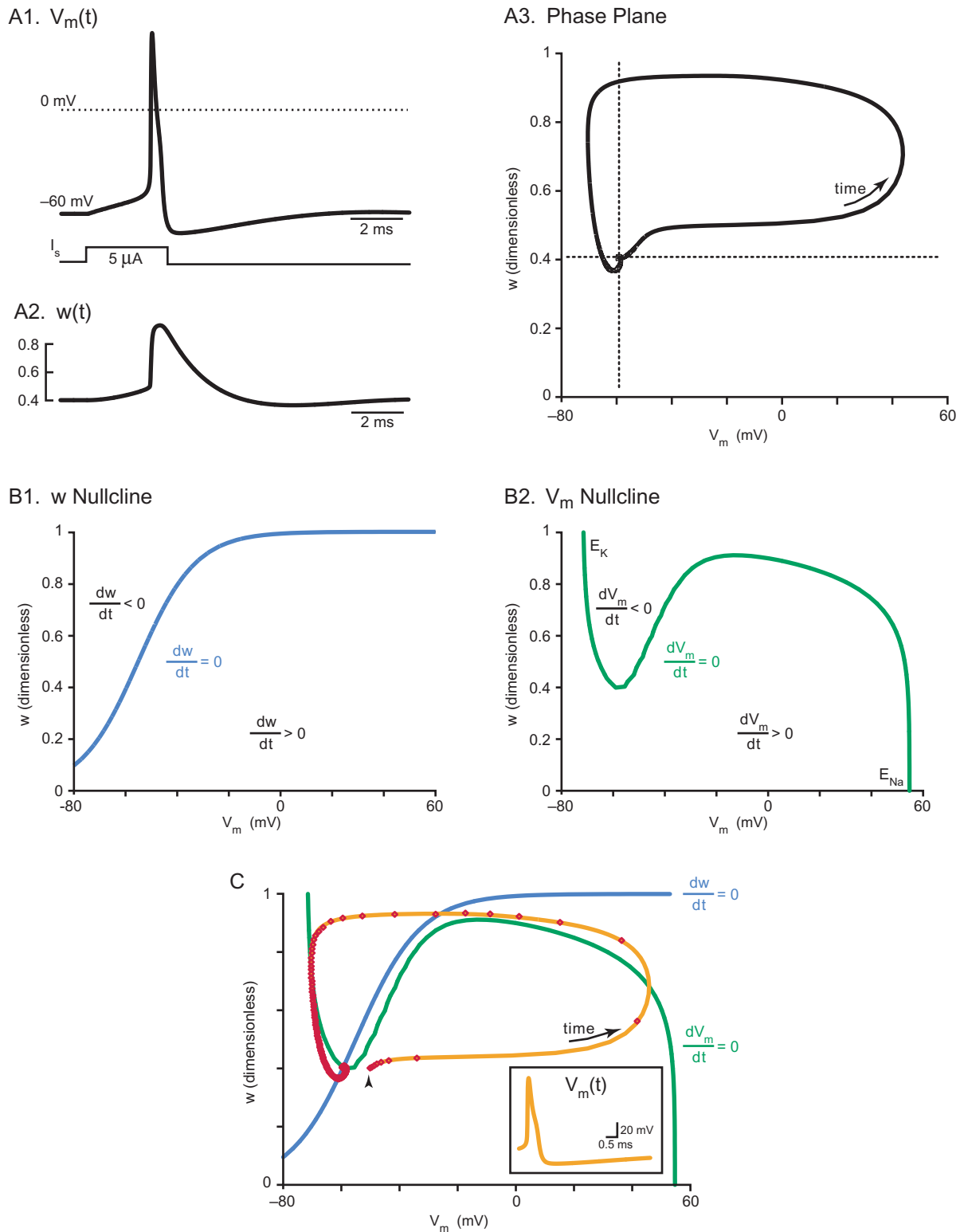


FIGURE 14.16 Two-dimensional model of neuronal excitability. The reduced model (Eqs. 14.49 and 14.50) is excitable and produces an action potential in response to a brief, suprathreshold stimulus. **A1:** Time-series plot of the computed membrane potential, $V_m(t)$. The resting membrane potential is -60 mV, and in response to a brief depolarizing current (i.e. $I_s = 5 \mu A \text{ cm}^{-2}$ for 3 ms; lower trace), the model produces an action potential. The parameters of the model (see below) were adjusted to closely approximate the squid giant axon. **A2:** Time-series plot of recovery variable, $w(t)$. At the resting potential, $w(t)$ has a value of ~0.4. During the action potential, the magnitude of $w(t)$ increases and this increase helps to restore the rest state. This variable acts much like the n and h gating variables of the Hodgkin and Huxley model (see

et al. (1991, 1993) and Av-Ron (1994) and by Canavier et al. (2002) to analyze the two-variable model described above (i.e., Eqs. 14.49 and 14.50).

The Action Potential Trajectory in the Phase Plane

Several methods can be used to visualize and analyze the dynamical behavior of the reduced model. For example, after numerically integrating the differential equations, the dependent variables (i.e., $V_m(t)$ and $w(t)$) can be plotted as a function of time (Fig. 14.16A1 and A2). Although this method of visualizing dynamical behavior may be familiar and is useful for comparing temporal relationship between the variables, it is not analytically powerful. A more valuable way to view the response of multiple variables is by *phase plane* profiles (i.e., curves of one dependent variable against another; Fig. 14.16A3). The solution path in the phase plane is referred to as a *trajectory*. The phase plane is completely filled with trajectories, since each point can serve as an initial condition for the model. For example, the simulation illustrated in Fig. 14.16A1–2, began with the initial conditions $V_m(0) = -59.407$ mV and $w(0) = 0.402$. This point is marked in the V_m - w plane by the dashed lines in Fig. 14.16A3. With these initial conditions the solution of the model does not change over time, i.e., the system is quiescent. Since there is no tendency for the variables to change, this point is referred to as a stable *fixed point* or *steady state*. If the system is subjected to a sufficiently large perturbation (e.g., a brief depolarizing current is injected), then the

solution path rapidly evolves along a curve in the phase plane (i.e., the black line in Fig. 14.16A3). This trajectory represents the evolution of an action potential in the V_m - w phase plane. Although time is not explicitly plotted in the phase plane, the direction of the solution is usually indicated by an arrow. The trajectory of the action potential begins and ends at the fixed point. Thus, this fixed point is an example of an *attractor*. Indeed, for the set of parameter values used in Fig. 14.16 and $I_s = 0$ μ A, all trajectories will ultimately return to this fixed point, which is said to be *globally attracting*.

To gain a more complete understanding of the dynamical behavior of the reduced model, it is useful to combine the phase plane profiles with a nullcline analysis. A *nullcline* for a given variable is a curve in the phase plane along which one of the derivatives is constant and is equal to zero. In addition, nullclines divide the phase plane into regions where the derivatives have a constant sign (see below). Nullclines for the reduced model are illustrated in Fig. 14.16B. The nullcline associated with the slow variable (i.e., w) is specified by the steady-state w curve (i.e., Eq. 14.54). If the system is currently located on the w nullcline, then its imminent trajectory must be horizontal, because only V_m can change (i.e., $dw/dt = 0$). Horizontal movements to the right of the w nullcline represent depolarizations, which in turn would cause w to increase. Conversely, horizontal movements to the left of the w nullcline represent hyperpolarization, which in turn would cause w to decrease. Thus, w is decreasing (i.e., $dw/dt < 0$) in the region to the left of the w nullcline and w is increasing (i.e., $dw/dt > 0$) in regions to the

Chapter 12). **A3:** The phase plane of the reduced model has coordinates V_m and w . The evolution of the variables is a point moving through this phase plane (black line). The direction of the trajectory (i.e., time) is indicated by the arrow. The values of w and V_m at the resting potential are indicated by the dashed lines. In the absence of any external stimulus, the trajectory (i.e., solution path) remains at the resting values of V_m and w (i.e., the intersection of the dashed lines). The brief increase in I_s (see Panel A1) displaces the trajectory away from the resting point. If the displacement crosses an apparent threshold along the V_m axis, the trajectory follows a large amplitude pseudo-orbit through the phase plane and back to the resting point. The large excursion of the trajectory represents the projection of the action potential in the phase plane. **B:** Nullclines of the reduced model. Nullclines in the phase plane are curves along which derivatives of a given variable are constant and equal to zero (i.e., $dV_m/dt = 0$, $dw/dt = 0$). In addition, nullclines divide the phase plane into regions where the derivatives have a constant sign. **B1:** w nullcline (blue line). The w nullcline specified by the steady-state function of w (Eq. 14.54). **B2:** V_m nullcline (green line). The V_m nullcline represents the pairs of values of $V_m(t)$ and $w(t)$ for which the net current is equal to zero (see Eq. 14.49). E_K and E_{Na} indicate the equilibrium potentials of I_{Na} and I_K . **C:** The trajectory of an action potential (yellow line) and the nullclines for V_m (green line) and w (blue line) are superimposed in the V_m - w plane. The intersection of the nullclines represents the resting point (i.e., quiescent state) in the phase plane. In response to an instantaneous displacement of system (arrow head) that crosses the threshold for generating an action potential, the system produces an action potential. Although time is not explicitly plotted in the phase plane, the red dots along the action potential trajectory are separated by 50 μ s. Thus, it is possible to visualize the speed of the solution path through the phase plane. The action potential trajectory passes through four regions in the phase plane. The initial up stroke of the spike (i.e., V_m is increasing) occurs in the region where both dV_m/dt and dw/dt are greater than zero. The trajectory crosses the V_m nullcline (i.e., the peak of the action potential) and enters a region where $dV_m/dt < 0$ (i.e., the falling phase of the action potential) and $dw/dt > 0$. As the trajectory crosses the w nullcline, it enters a region where both dV_m/dt and dw/dt are less than zero (i.e., the absolute refractory period; see Chapter 12). Finally, the trajectory crosses the V_m nullcline a second time (i.e., the minimum of the after hyperpolarization) and enters a region where $dV_m/dt > 0$ and $dw/dt < 0$ (i.e., the relative refractory period; see Chapter 12). **Insert:** the time-series plot of $V_m(t)$ that is equivalent to the trajectory in the phase plane. For these simulations $C_m = 1$ μ F/cm², $\bar{g}_{Na} = 120$ mS/cm², $\bar{g}_K = 36$ mS/cm², $\bar{g}_l = 0.3$ mS/cm², $E_{Na} = 55$ mV, $E_K = -72$ mV, $E_l = -49.4$ mV, $V_{1/2}^{(m)} = -33$ mV, $V_{1/2}^{(w)} = -55$ mV, $a^{(m)} = 0.055$, $a^{(w)} = 0.045$, $mp = 3$, $wp = 4$, $s = 1.3$ and $\bar{\lambda} = 0.2$. With these parameters, the reduced model simulates the properties of the squid giant axon. Adapted from Av-Ron et al. (1991).

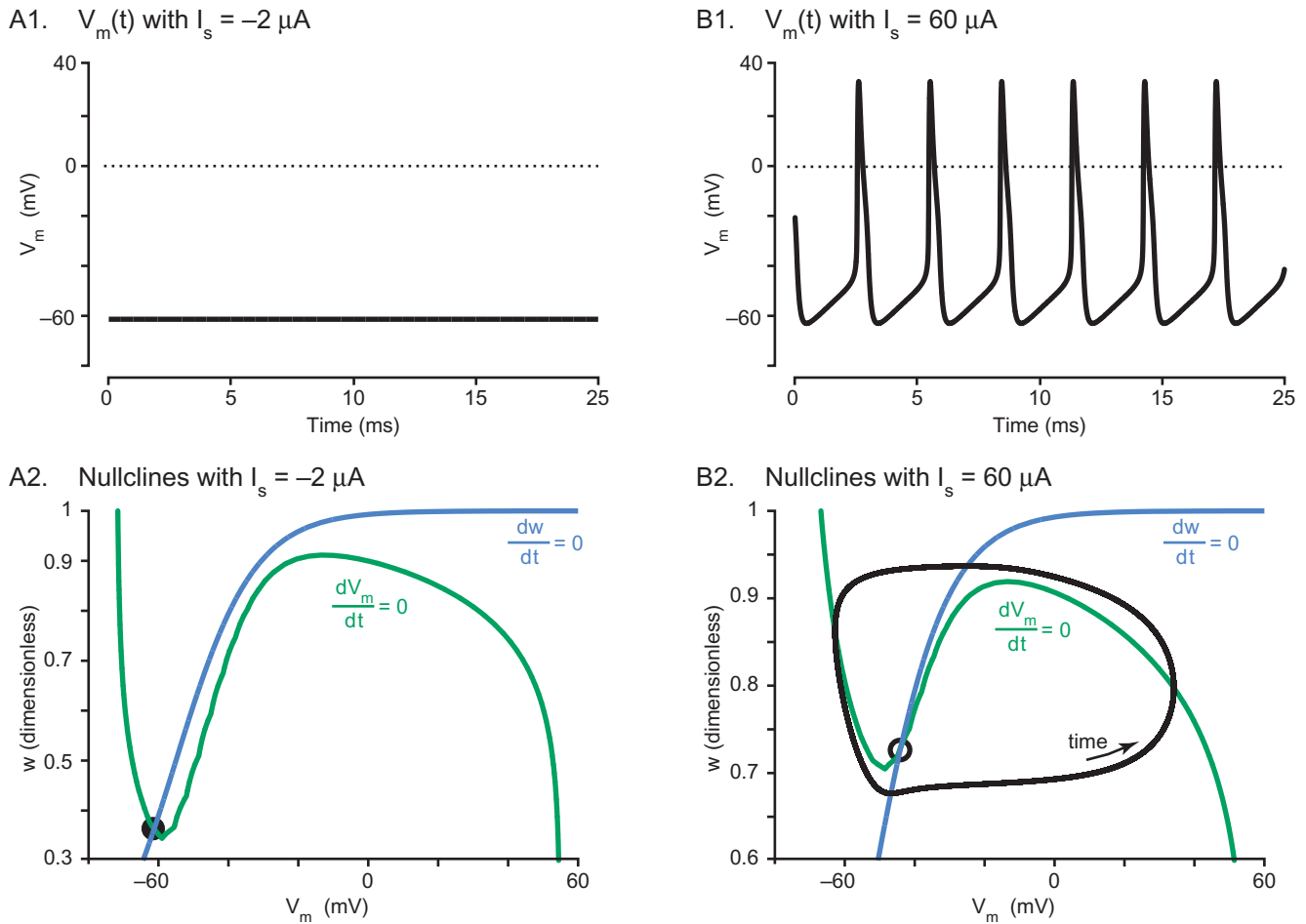


FIGURE 14.17 Oscillations emerge as fixed points lose stability. In a phase plane, the intersection of nullclines defines a fixed point (i.e., $dV_m/dt = dw/dt = 0$). Fixed points can be either stable or unstable. **A1:** When the value of $I_s = -2 \mu\text{A cm}^{-2}$, the computed membrane potential is quiescent. Although sufficiently large perturbation will elicit an action potential (not shown), the system will ultimately return to the stable resting state. **A2:** The fixed point is indicated with a filled black circle and it occurs on a stable branch of the V_m nullcline (green line). Thus, the fixed point is stable. **B1:** When the value of $I_s = 60 \mu\text{A cm}^{-2}$, the computed membrane potential is oscillating (i.e., repetitive spiking). Although perturbations may transiently alter this pattern of firing, the system will ultimately return to this exact pattern of repetitive spiking. **B2:** the fixed point (open circle at the intersection of the nullclines) is now located on the unstable branch of the V_m nullcline, and thus, the resting state is not stable. The closed curve (black line) represents the trajectory of the system in the phase plane and corresponds to a stable limit cycle. With the exception of I_s , all values for parameters were as in Fig. 14.16.

right of the w nullcline. The nullcline associated with the fast variable (i.e., V_m) is a cubic function (Fig. 14.16B2), and is composed of pairs of values of $V_m(t)$ and $w(t)$ for which the net current is equal to zero (see Eq. 14.49). If the evolution of the system brings it onto the V_m nullcline, its imminent trajectory must be vertical, because only w can change (i.e., $dV_m/dt = 0$). Downward vertical movements represent a decrease in w , which in turn would cause V_m to increase (see Eq. 14.51). Conversely, upward vertical movements represent an increase in w , which in turn would cause V_m to decrease. Thus, V_m is decreasing (i.e., $dV_m/dt < 0$) in regions above the V_m nullcline, and, V_m is increasing (i.e., $dV_m/dt > 0$) in regions

below the V_m nullcline. Given that the rate of change of V_m is fast compared to that of w , the nullclines define two very important features of the phase plane. First, the fixed points of the system can be predicted from the nullclines. At intersections of the nullclines (i.e., $dV_m/dt = dw/dt = 0$), there is no tendency for any variable to change, so these intersections represent fixed points or steady states. A fixed point does not guarantee a quiescent membrane potential, however. Fixed points may not be stable to small perturbations (see below). Second, the qualitative dynamics of the system can be predicted from the nullclines. The qualitative prediction is possible because the system will quickly relax to near the potential nullcline, then

BOX 14.4

FIXED POINTS AND BIFURCATIONS IN NONLINEAR DYNAMICAL SYSTEMS

Systems that change, that evolve in time, are referred to as *dynamical systems*. Mathematical representations of dynamical systems fall into two general categories: *difference equations* (or *iterative maps*) and *differential equations*. Iterative maps are used to represent systems where time is taken to be discrete, whereas differential equations are used to represent systems where time is taken to be continuous. Differential equations are widely used in science and engineering. The two most common types of differential equations are *ordinary differential equations* (ODEs) in which there is only one independent variable (e.g., time, t), and *partial differential equations* in which there are two or more independent variables such as time (t) and space (x). Both types of differential equations were used by Hodgkin and Huxley to model action potentials (i.e., the spaced-clamped versus the propagated action potential). The solution and analysis of partial differential equations is complex, however. Thus, ODEs are more commonly used and there are many tools available to investigate and understand the dynamical behavior of ODEs (Abraham and Shaw, 1992; Ermentrout, 1996, 2000; FitzHugh, 1969; Izhikevich, 2000; Jackson, 1991; Pavlidis, 1973; Strogatz, 1994; Tufillaro et al., 1992).

Dynamical systems are described in terms of how many differential equations are included in the system (i.e., an “ n th-order” or “ n -dimensional” system) and whether they are *linear* or *nonlinear*. For example, consider the following general system:

$$\frac{dx}{dt} = k_1x_1 + k_2x_2 \quad (14.57)$$

$$\frac{dx_2}{dt} = k_3x_1 + k_4x_2 \quad (14.58)$$

where k_i are constants and x_i are variables. This is a second-order or two-dimensional system, because there are two ODEs. In addition, these ODEs are referred to as coupled because x_1 is defined in terms of x_2 , and vice versa. This is also a linear system, because all of the x_i on the right-hand side appear to the first power only (see also Chapter 6). Otherwise, the system would be nonlinear. Typical nonlinear terms are products (e.g., $x_i x_j$), powers (e.g., x_i^3) and functions (e.g., $\sin x_i$).

Unlike linear systems (e.g., Eqs. 14.57 and 14.58), most nonlinear systems are impossible to solve analytically, and must be studied by using techniques such as numerical integration of the equations, geometric methods such as phase plane analysis, and stability theory.

For example, consider a general form for a nonlinear, two-dimensional system:

$$\frac{1}{\mu} \frac{dx_1}{dt} = f_1(x_1, x_2) \quad (14.59)$$

$$\frac{dx_2}{dt} = f_2(x_1, x_2) \quad (14.60)$$

where the functions f_1 and f_2 are determined by the problem at hand and x_1 and x_2 are variables. For example, f_i may describe processes underlying neuronal excitability, and the variables x_1 and x_2 might represent membrane potential, gating variables for membrane conductances or the intracellular concentration of a second messenger. The parameter μ can be thought of as a rate constant that scales the relative rates of the two functions. When $0 < \mu \ll 1$, then Eq. 14.59 is referred to as the slow subsystem and Eq. 14.60 is referred to as the fast subsystem. Numerical integration of Eqs. 14.59 and 14.60 will produce a set of ordered pairs of real numbers $x_1(t)$ and $x_2(t)$; where $x_1(0)$ and $x_2(0)$ represent the initial values (i.e., *initial conditions*) of the two variables (i.e. at time $t = 0$) and $x_1(t)$ and $x_2(t)$ represent the values of the two variables at time t (i.e., the *temporal evolution* of the variables). A common method for visualizing these solutions is to plot $x_1(t)$ and/or $x_2(t)$ versus time (e.g., Figs. 14.16A1 and A2). Such a plot is referred to as a *time series* plot of the variables. Alternatively, an abstract space with coordinates (x_1, x_2) can be constructed. In this space, the solution $(x_1(t), x_2(t))$ corresponds to a point moving along a curve (e.g., Fig. 14.16A3). This curve (i.e., the solution to the system of differential equations) is referred to as a *trajectory*, and the direction of motion along a trajectory is often indicated by an arrowhead. The abstract space is called the *phase space* for the system, and the *phase portrait* of the system shows the overall picture of trajectories in phase space. Because Eqs. 14.59 and 14.60 constitute a two-dimensional system, the phase space of the system is a plane (i.e. a *phase plane*).

If a trajectory asymptotically approaches a constant, time-independent solution, then this point in the phase space is referred to as a *stable fixed point* (e.g., Fig. 14.17A2). (Note, dynamical systems theory is rife with conflicting terminology and different terms are often used for the same thing. For example, fixed points are also referred to as points of equilibrium, or singularities, or critical points. This lack of a standard terminology can be a source of great frustration and confusion for individuals

BOX 14.4 (cont'd)

not intimately involved in the field of dynamical systems theory.) In the phase plane, stable fixed points often are indicated by solid black dots. Alternatively, if a trajectory of a nonlinear system asymptotically approaches a time-dependent solution that precisely returns to itself in a time T (i.e., the period), then this periodic solution is referred to as a *stable limit cycle* or simply a *limit cycle* (e.g., Fig. 14.17B2). A limit cycle is represented as a closed curve on a phase plane. These two asymptotically stable trajectories (i.e. stable fixed point and limit cycle) are examples of *attractors*, because trajectories approach and coalesce on them. If a phase plane has only one attractor, then all trajectories ultimately lead to that solution, which is referred to as *globally attracting* (e.g., Fig. 14.16C). Alternatively, if a phase plane has more than one attractor, then the system can manifest more than one stable steady state and, thus, is referred to as *multistable* (e.g., Fig. 14.19B; see also Chapter 6).

Because of the special topological properties of the plane, phase plane analyses can provide fundamental insights into the dynamical properties of a two-dimensional system such as Eqs. 14.59 and 14.60. For example, the Jordan Curve Theorem implies that the only attractors in the phase plane are limit cycles and fixed points. The fixed points in a phase plane can be identified by plotting the *nullclines* (e.g., Fig. 14.16B). A nullcline is a curve in the phase plane along which the rate of change of a particular variable is zero (i.e., $dx_i/dt = 0$). Nullclines are useful because they separate the phase plane into regions in which the derivative of each variable has a constant sign and because any place the two nullclines intersect is a fixed point (i.e., $dx_1/dt = dx_2/dt = 0$).

Fixed points have several features that can be used to classify them. For example, a fixed point can be either *stable* (e.g., Fig. 14.17A2) or *unstable* (e.g., Fig. 14.17B2). A fixed point is stable if all sufficiently small perturbations away from it dampen out with time (i.e., the solution returns to the fixed point). Alternatively, if the perturbation grows with time, the fixed point is unstable. The stability of fixed points can be defined more rigorously in mathematical terms, and readers who want a more detailed discussion of this matter should consult one of the many excellent textbooks that deal with nonlinear systems (e.g., Strogatz, 1994).

In addition to stability, fixed points can be classified on the basis of how trajectories behave in the neighborhood of the fixed point. Such behavior is often referred to as the *flow* or *motion*. For example, trajectories approach *stable nodes* and leave *unstable nodes*. Trajectories in the neighborhood of the *saddle point* are hyperbolic (i.e., they do not approach the saddle point,

but pass by it, looking somewhat like members of a family of hyperbolas near their common center). Saddle points organize boundaries (i.e., a *threshold separatrix*) between classes of trajectories with qualitatively different properties. For example, on one side of the separatrix may reside a stable node that represents a quiescence or rest state (e.g., the resting membrane potential of a neuron), and on the other side may reside a large amplitude trajectory that starts and ends near the equilibrium (e.g., a spike). Thus, small perturbations of the solution decay if they do not lead beyond the separatrix, whereas those crossing the separatrix grow away exponentially. A system with a saddle point has well-defined threshold and all-or-none behavior. Because the solution eventually returns to the stable node (i.e., rest state), however, the system is not oscillatory, but rather it is excitable. Thus, a saddle point can be used to describe threshold phenomenon mathematically.

Fixed points and closed orbits can be created or destroyed or destabilized as parameters are varied. If the phase portrait changes its topological structure as a parameter is varied, this is termed a *bifurcation*. Examples include changes in the number or stability of fixed points, closed orbits, or saddle connections as a parameter is varied. Bifurcations are most clearly illustrated in what is termed a *bifurcation diagram* (e.g., Fig. 14.18B). A *bifurcation diagram* plots a system parameter (e.g., μ in Eq. 14.59), which is referred to as the *bifurcation parameter*, on the horizontal axis and a representation of an attractor (e.g., x_i in Eqs. 14.59 and 14.60) on the vertical axis (see also Chapter 6). As the value for the parameter is systematically varied the stability of the fixed points (and closed orbits) will change, which is usually indicated by a branch in the bifurcation diagram. Bifurcations are important, because they provide insights into when transitions and instabilities may occur as some control parameter is varied.

For those who wish to explore the behavior of dynamical systems, dynamical systems software has recently become available for personal computers. In general, with these software packages, all one has to do is type in the equations and the parameters; the program solves the equations numerically and provides analytical tools. For example, the software package XPPAUT can plot variables in two- and three-dimensional phase space, calculate and plot nullclines, analyze the stability of fixed points and perform bifurcation analyses (Ermentrout, 2002). The features and availability of several of these software packages were recently reviewed (Brette et al., 2007; Ermentrout, 2002; Hayes et al., 2002; Hubbard and West, 1992; Kocak, 1989).

move in the direction dictated by whether w , the slow variable, is increasing or decreasing. Furthermore, the stability of a fixed point can be predicted based on which branch of the V_m nullcline contains it (under the assumption that voltage changes much more rapidly than w). In the middle branch, positive feedback dominates so a fixed point in the branch is unstable with respect to perturbations. The other branches are stable. For the system to be excitable or oscillatory, w must be decreasing above the w nullcline (left stable branch) and increasing below it (right stable branch). This will cause a loop in the trajectory as shown in Fig. 14.16C.

The configuration of the nullclines can be changed by altering values of the parameters. For example (Fig. 14.17), the nullclines can be altered by varying the parameter I_s (i.e., the externally applied stimulus current). If the value of I_s is set to $-2 \mu\text{A cm}^{-2}$, the system is quiescent (Fig. 14.17A1). In the quiescent case, the single fixed point (filled circle in Fig. 14.17A2) falls on the left branch of the V_m nullcline and thus is stable. Although the system is quiescent, it remains excitable, and a sufficiently large perturbation will elicit an action potential (e.g., Fig. 14.16A1). If the value of I_s is set to $60 \mu\text{A cm}^{-2}$, the dynamical behavior of the system is qualitatively different. The system continuously generates action potentials with a constant inter-spike interval (Fig. 14.17B1). This type of activity is often referred to as *beating* or *pacemaker activity*. In the pacemaker case, the fixed point is moved onto the unstable middle branch (open circle in Fig. 14.17B2). Thus, rather than returning to a single point in the phase plane, the solution path continually travels along a closed curve in the phase plane (black line in Fig. 14.17B2), which is referred to as a *limit cycle*. This limit cycle is stable, and if the system is momentarily perturbed, the trajectory will only transiently leave the limit cycle. Regardless of the magnitude of the perturbation, the solution path will ultimately return to the limit cycle.

Bifurcations and Bistability

A nonlinear system can make a transition from a stable fixed point to a limit cycle in several ways (for reviews see Izhikevich, 2000; Qi et al., 2013). Such transitions are termed *bifurcations*. A bifurcation occurs any time the phase portrait (i.e., the overall picture of trajectories in the phase space) is changed to a topologically nonequivalent portrait by a change in the value of a control or *bifurcation parameter*. For example, increasing I_s from $0 \mu\text{A}$ to $60 \mu\text{A}$ causes the reduced model to transition (i.e., a bifurcation) from a resting state to an oscillatory state (Fig. 14.18A). In the phase

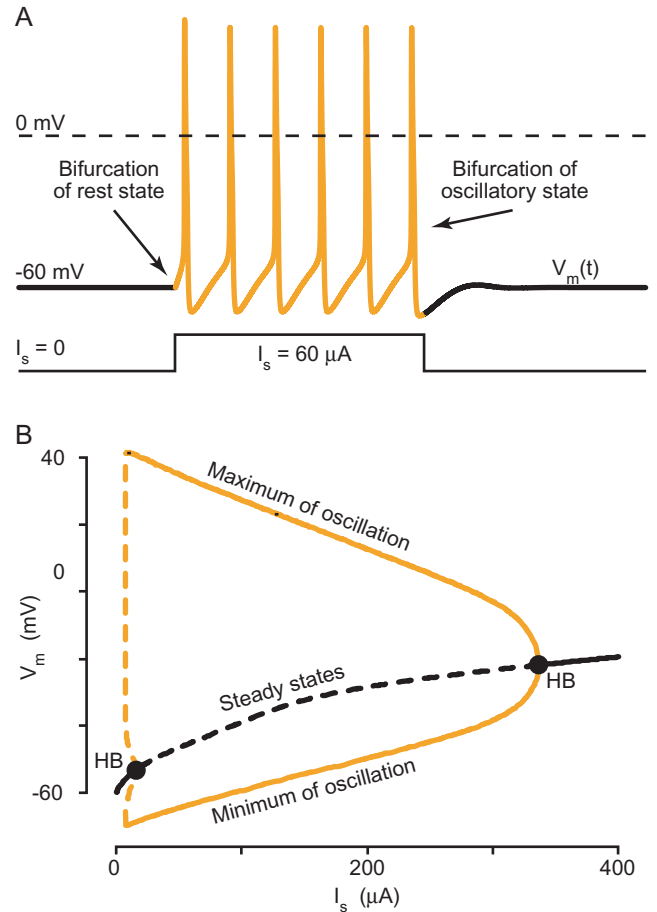


FIGURE 14.18 Bifurcations between quiescent and oscillatory states. As parameters are changed, nonlinear systems can make transitions between a stable steady state (i.e., a quiescent state) and a limit cycle (i.e., oscillations). These transitions are referred to as bifurcations. **A:** When $I_s = 0 \mu\text{A cm}^{-2}$, the system is in a stable steady state. When $I_s = 60 \mu\text{A cm}^{-2}$, the resting state loses stability and stable oscillations emerge. If I_s is returned to $0 \mu\text{A cm}^{-2}$, the periodic solution loses stability, and the system returns to a stable steady state. With the exception of I_s , all values for parameters were as in Fig. 14.16. **B:** A bifurcation diagram plots the steady states (black line) of a system as the value of a parameter is systematically varied. Stable steady states are indicated by solid line and unstable steady states are indicated by dashed line. For values of I_s between 0 and $16.31 \mu\text{A cm}^{-2}$, the steady state is stable and the system is quiescent. At $I_s = 16.31 \mu\text{A cm}^{-2}$, however, the steady state loses stability and oscillations emerge. The mathematical characteristics of this bifurcation classify it as a Hopf bifurcation (point HB). For a review of the mathematical criteria used to classify various types of bifurcations, see Strogatz (1994). The periodic solution loses stability as $I_s > 336.8 \mu\text{A cm}^{-2}$, and once again the system is quiescent (i.e., the steady state is stable). The second transition is also a Hopf bifurcation. In addition to the steady states, the bifurcation diagram plots the maximum and minimum values of V_m during periodic solutions (yellow line). Periodic solutions also can be either unstable (dashed line) or stable (solid line). With the exception of I_s , all values for parameter were as in Fig. 14.16. In this and subsequent figures, the bifurcation analyses were performed using the AUTO (Doedel, 1981) algorithm, which is incorporated into the XPPAUT software package (Ermentrout, 2002).

portrait, this transition would represent the loss of a stable fixed point (e.g., Fig. 14.17A2) and the emergence of a stable limit cycle (e.g., Fig. 14.17B2). Conversely, if I_s is decreased from $60 \mu\text{A cm}^{-2}$ to $0 \mu\text{A cm}^{-2}$, there is a bifurcation of the oscillatory state, which is represented in the phase portrait as a loss of the stable limit cycle and the emergence of a stable fixed point.

The bifurcation is most clearly illustrated in what is termed a *bifurcation diagram* (Fig. 14.18B; see also Chapter 6). A bifurcation diagram plots a system parameter (e.g., I_s) on the horizontal axis and a system variable (e.g., V_m) on the vertical axis. For example, in Fig. 14.18B, the value of I_s was systematically increased from 0 to $400 \mu\text{A cm}^{-2}$. At each new value of I_s , the steady-state value of V_m (i.e., the value of V_m at the fixed point) was determined and the stability of the fixed point was determined. For values of I_s between 0 and $16.31 \mu\text{A cm}^{-2}$ the fixed point is stable, which is indicated by the solid black line. At $I_s = 16.31 \mu\text{A cm}^{-2}$, the fixed point loses stability and a periodic solution emerges (i.e., a bifurcation). The transition illustrated in Fig. 14.18 is a type of bifurcation known as a Hopf bifurcation (filled circle labeled HB). For values of I_s between 16.31 and $336.8 \mu\text{A cm}^{-2}$, the fixed point remains unstable, as indicated by the dashed black line. At $I_s = 336.8 \mu\text{A cm}^{-2}$, the periodic solution loses stability and a stable fixed point emerges, again via a Hopf bifurcation. The fixed point remains stable for all further increases in I_s .

Figure 14.18B also illustrates the maximum and minimum values of V_m for the oscillatory response (the yellow lines). Just as a fixed point can be stable or unstable, a periodic solution can also be stable or unstable. The unstable periodic solutions are indicated by the dashed, yellow line and the stable limit cycles are indicated with the solid yellow line. When a Hopf bifurcation leads to *unstable* periodic solutions (i.e., the Hopf bifurcation that occurs at $I_s = 16.31 \mu\text{A}$), then the bifurcation is termed *subcritical* (Fig. 14.19A1). When a Hopf bifurcation leads to only *stable* periodic solutions (i.e., the Hopf bifurcation that occurs at $I_s = 336.8 \mu\text{A cm}^{-2}$), it is termed *supercritical* (Fig. 14.19A2). The two Hopf bifurcations are illustrated in greater detail in Fig. 14.19. The supercritical Hopf bifurcation is the simpler type, and because of its appearance in a bifurcation diagram, is also referred to as a pitchfork bifurcation. At the supercritical Hopf bifurcation, the amplitude of the periodic solution slowly decreases in amplitude until a stable steady state is reached. This lethargic decay is called “critical slowing down” in the physics literature (Strogatz, 1994). In contrast to the supercritical Hopf bifurcation, the subcritical Hopf bifurcation has a relatively complex configuration (Fig. 14.19A1). The emergent branches of the unstable periodic solutions (dashed yellow lines) fold

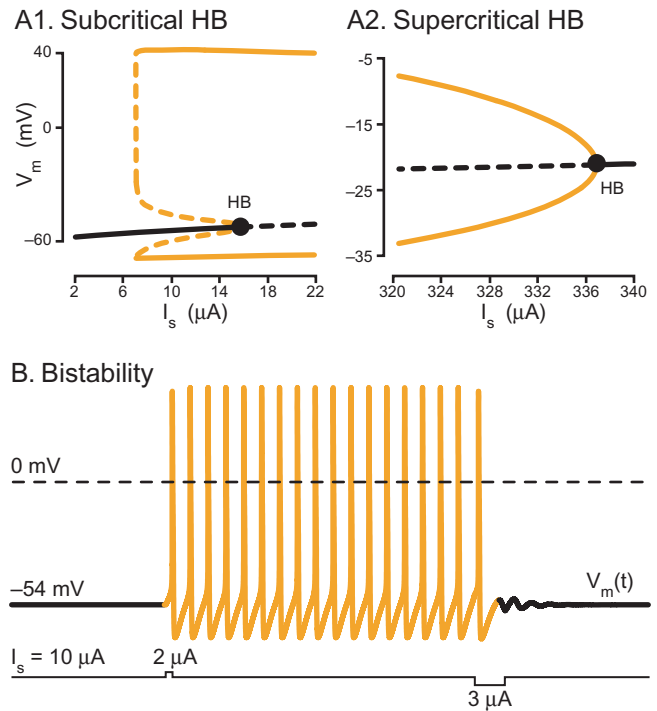


FIGURE 14.19 Bistability. In a nonlinear system, it is possible for more than one stable solution to coexist in a given parameter regime. Thus, the system is said to be bistable (i.e., two stable solutions) or multistable (more than two stable solutions). For an example of a multistable system see Canavier et al. (1993) and Butera (1998). **A:** The regions of the two Hopf bifurcations in Fig. 14.18 are expanded and plotted. **A1:** The first Hopf bifurcation (i.e., $I_s = 16.31 \mu\text{A cm}^{-2}$) is a subcritical Hopf bifurcation. The unstable branch of the periodic solution folds back over a region in which the steady state is stable. This results in a parameter region where the stable steady state and stable periodic solution overlap. Thus, the system can reside on either of the two stable attractors and perturbations can switch the system between the two stable states (see below). **A2:** The second Hopf bifurcation is a supercritical Hopf bifurcation. The amplitude of the periodic solution decreases in amplitude through exponentially damped oscillations. **B:** At the beginning of the simulation, the system resides in a stable resting state. A brief perturbation (see trace labeled I_s), however, induces a switch from the stable resting state to the stable oscillatory state. A second perturbation can switch the system back to the stable resting state. At a subcritical Hopf bifurcation, the trajectory can be induced to ‘jump’ between distant attractors. Thus, large amplitude oscillations appear dramatically from the resting state. With the exception of I_s , all values for parameter were as in Fig. 14.16. At the beginning of the simulation (i.e., at $t = 0$), the values for the two state variables (i.e., $V_m(t)$ and $w(t)$) were initially set to $V_m(0) = -54.314 \text{ mV}$ and $w(0) = 0.515$. The values of state variables at the beginning of a simulation are referred to as the *initial conditions*.

back into the parameter region where the steady state is stable. This backward folding has several important implications. First, because of this backward fold, there is a parameter region where the stable fixed points (i.e., solid black line) and the stable limit cycle (i.e., solid yellow lines) overlap. In this parameter region, the model is *bistable*, i.e., both a stable quiescent and a stable oscillatory solution coexist (see also Chapter 6).

In the phase plane (not shown), this type of bistability would be represented by a stable fixed point at the intersection of the nullclines, and surrounding the stable fixed point would first be an unstable period orbit and then a stable limit cycle. Note, bistability can result from other types of bifurcation schema, which in turn would have different properties and different phase plane portraits. For some examples of different mechanisms for achieving bistability, see Bertram et al. (1995), Canavier et al. (2002), Izhikevich (2000), or Rinzel and Ermentrout (1998). Second, the existence of different stable states allow for the possibility of “jumps” between the two stable states and of hysteresis (i.e., the lagging of an effect behind its cause). Finally, as the solution jumps from the stable steady state to the stable periodic solution, large amplitude oscillations appear dramatically from the resting state. In the physics literature, this dramatic jumping between states is referred to an “explosive instability” or a “blow-up” (Strogatz, 1994).

Bistability can endow a neuron with some very interesting dynamical properties. For example, in the bistable regime, sufficiently large perturbations can induce a jump or switch from a resting state (i.e., stable steady solution) to a spiking state (i.e., stable oscillatory state) and vice versa. Figure 14.19B illustrates such a case. At the beginning of the simulation (i.e., at $t=0$), the values for the two state variables (i.e., $V_m(t)$ and $w(t)$) were initially set to $V_m(0) = -54.314$ mV and $w(0) = 0.515$. The values of state variables at the beginning of a simulation are referred to as the *initial conditions*. With these initial conditions and parameter values, the system resides on the stable fixed point and is quiescent (black line in the $V_m(t)$ trace of Fig. 14.19A). In the absence of any large perturbations, the system will remain in this resting state indefinitely. However, a sufficiently large perturbation (e.g., a $2 \mu\text{A cm}^{-2}$, 3 ms injection of current) can send the solution path off the stable fixed point and onto the stable limit cycle. In the absence of any large perturbations, the system will remain in the oscillatory state indefinitely. However, a sufficiently large perturbation (e.g., a $-3 \mu\text{A cm}^{-2}$, 12 ms injection of current) can send the solution path off the stable limit cycle and back onto the stable fixed point. Such behavior has been observed empirically, for example in the squid giant axon (Guttman et al., 1980) and in the bursting neuron R15 of *Aplysia* (Lechner et al., 1996). The switch from the resting state to the oscillatory state is often referred to as *hard excitation* and the switch from the oscillatory state to the resting state is often referred to as *annihilation*. Moreover, this bistable behavior is critical for the occurrence of bursting when a slow conductance is added to the system (see below).

Dynamical Underpinnings of Bursting Activity

In contrast to pacemaker activity (i.e., continuous spiking activity with an approximately constant interspike interval), *bursting activity* is characterized by the clustering of spikes into groups that are separated by quiescent periods. Bursting cells can be classified as conditional or endogenous bursters. *Endogenous bursters* fire in a bursting pattern in the absence of any input, whereas *conditional bursters* can fire in bursts if they receive appropriate input from other neurons within a network. Endogenous bursting activity relies on bistability in the system.

In the example of bistability described previously (Fig. 14.19), the bifurcation parameter was an externally applied current. Other, more physiologically relevant, parameters can achieve similar results. For example, adjusting the magnitude of an ionic conductance such as \bar{g}_K (i.e., the maximal conductance of I_K ; see Eq. 14.52) can alter the dynamical properties of the system (Av-Ron et al., 1991). Fig. 14.20 illustrates a bifurcation diagram in which \bar{g}_K was used as the bifurcation parameter. As the value of \bar{g}_K is decreased, the steady state loses stability and an oscillatory state emerges via a subcritical Hopf bifurcation. This oscillatory state represents the pacemaker activity, which is similar to that illustrated in Fig. 14.17B1. With further

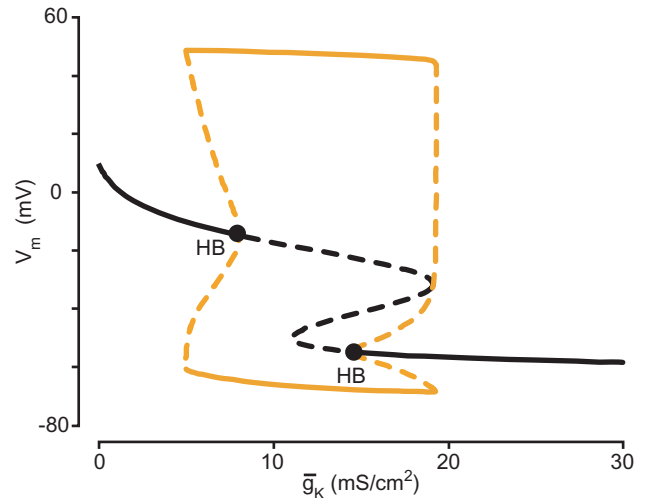


FIGURE 14.20 Bifurcation diagram as a function of \bar{g}_K . As in previous bifurcation diagrams stable solutions are indicated by solid lines and unstable solutions are indicated by dashed lines. The steady states are indicated by the black line and the periodic solutions are indicated by the yellow line. Moving from right to left along the X axis, the maximum conductance for the K^+ current (i.e., \bar{g}_K) decreases. As \bar{g}_K is decreased, the steady state loses stability and oscillations emerge via a subcritical Hopf bifurcation (point HB). As \bar{g}_K continues to decrease, the periodic solution loses stability and a stable steady state emerges via a second subcritical Hopf bifurcation. With the exception of \bar{g}_K , all values for parameters were as in Fig. 14.16. Adapted from Av-Ron et al. (1991).

reductions in \bar{g}_K , the oscillatory state loses stability and a stable steady state emerges via a subcritical Hopf bifurcation. Thus, there are two parameter regions where bistability exists, and in principle, the system could be made to burst if the value of \bar{g}_K was forced to traverse back and forth between parameter regions associated with a stable steady state and a stable limit cycle.

Generally, bursting cannot occur in a two-variable model (Rinzel and Ermentrout, 1998). Bursting can be realized, however, by incorporating an additional process (i.e., a relatively slow negative feedback process). To illustrate the general principles underlying burst firing, the reduced model presented previously (i.e., Eqs. 14.49 and 14.50) is extended to include two more currents (I_{Ca} and $I_{K,Ca}$; see also Chapters 12 and 13) and an additional variable ($[Ca^{2+}]$), which describes the intracellular concentration of Ca^{2+} . Although several schema are possible, the two additional currents considered here are an inward Ca^{2+} current (I_{Ca}) that activates with increasing depolarization, and an outward K^+ current that is activated by intracellular Ca^{2+} ($I_{K,Ca}$). The two new currents are described by:

$$I_{K,Ca} = \bar{g}_{K,Ca} z([Ca^{2+}]) (V_m - E_K) \quad (14.61)$$

$$I_{Ca} = \bar{g}_{Ca} m_{\infty}^{mp}(V_m) (1 - w(V_m, t)) (V_m - E_{Ca}) \quad (14.62)$$

where \bar{g}_i represents the maximal conductances of the ionic currents, E_i represents their respective equilibrium potentials, and z is a function that describes the Ca^{2+} -dependency of the $I_{K,Ca}$, which is given by:

$$z([Ca^{2+}]) = \frac{[Ca^{2+}]}{[Ca^{2+}] + K_d} \quad (14.63)$$

where $[Ca^{2+}]$ represents the concentration of intracellular Ca^{2+} and K_d is the concentration at which $I_{K,Ca}$ is half activated. The dynamics of intracellular Ca^{2+} are described by:

$$\frac{d[Ca^{2+}]}{dt} = K_p(-I_{Ca}) - R[Ca^{2+}] \quad (14.64)$$

where K_p is a conversion factor from current to concentration and R is the removal rate constant. (See Chapter 6 for more detailed models of Ca^{2+} regulation.) Note that by extending Eq. 14.49 to include $I_{K,Ca}$, the total K^+ conductance of the reduced model becomes:

$$g_K^{(total)} = \bar{g}_K \left(\frac{w(V_m, t)}{s} \right)^{wp} + \bar{g}_{K,Ca} z([Ca^{2+}]) \quad (14.65)$$

The conductances \bar{g}_K and $\bar{g}_{K,Ca}$ are determined such that the system traverses a region of bistability (see

Fig. 14.20). For additional details, see Av-Ron et al. (1991, 1993).

Fig. 14.21 illustrates a bursting solution to the three-variable model (Eqs. 14.49, 14.50 and 14.64). During the quiescent phase, V_m (Fig. 14.21A) ramps up and fast subthreshold oscillations give rise to a burst of action potentials. During the burst of action potentials, $[Ca^{2+}]$ increases (Fig. 14.21B), which in turn increases the magnitude of $I_{K,Ca}$ (Fig. 14.21C). Once $\bar{g}_K^{(total)}$ becomes sufficiently large, the oscillation is halted. Calcium is removed during the quiescent period,

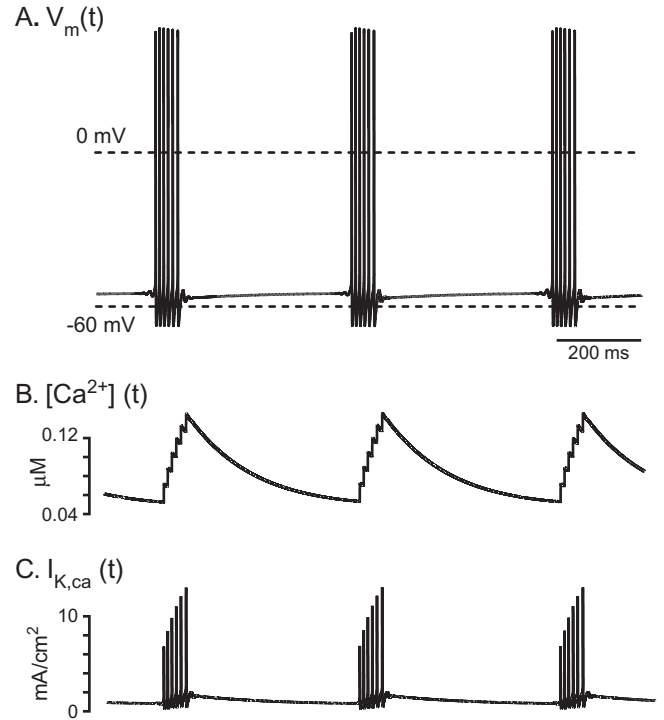


FIGURE 14.21 Elliptic (Type III) bursting in a three-dimensional model. In the absence of any external stimulus, the three-variable model generates sustained bursting activity. **A:** Time-series plot of the computed membrane potential ($V_m(t)$). Brief bursts of action potentials are separated by quiescent periods. Small subthreshold oscillations can be seen waxing and waning before and after each burst of spikes. **B:** Time-series plot of the computed intracellular concentration of Ca^{2+} ($[Ca^{2+}](t)$). Calcium enters the cell during the spikes and slowly accumulates during the burst. During the intervening quiescent period, the levels of Ca^{2+} fall. Note the slow time scale with which levels of Ca^{2+} vary. **C:** Time-series plot of $I_{K,Ca}(t)$ during the bursting activity. As Ca^{2+} accumulates during the burst (see Panel B), the magnitude of $I_{K,Ca}$ increases. Once the total K^+ conductance (see Eq. 14.65) is sufficiently large, the spiking activity is terminated. As the level of Ca^{2+} slowly decreases (see Panel B) during the quiescent period, $I_{K,Ca}$ begins to decrease. Once the total K^+ conductance has decreased sufficiently, spiking resumes. This cycle of events repeats indefinitely and does not require an external stimulus. Thus, this bursting activity is intrinsic (or endogenous) to the system. With the exception of $\bar{g}_{Ca} = 5 \text{ mS/cm}^2$, $E_{Ca} = 124 \text{ mV}$, $\bar{g}_K = 12 \text{ mS/cm}^2$, $E_K = -50 \text{ mV}$, $\bar{g}_{K,Ca} = 0.5 \text{ mS/cm}^2$, $K_d = 0.5 \text{ mM}$, $K_p = 0.00052$, and $R = 0.0045$, all values for parameter were as in Fig. 14.16. Adapted from Av-Ron et al. (1993).

BOX 14.5

ALTERNATIVE MODELS OF EXCITABILITY

Over the past 50 years, the formalisms developed by Hodgkin and Huxley have been used as a starting point for developing conductance-based models. These models were usually developed to simulate specific systems, such as the endogenous bursting cell R15 in *Aplysia* (Canavier et al., 1991) or the thalamocortical relay neurons (McCormick and Huguenard, 1992; Pospichil et al., 2008). These models often incorporate descriptions of three to ten ionic conductances and may include additional variables that describe processes such as the dynamics of intracellular levels of Ca^{2+} or the dynamics of a second messenger such as cAMP. Thus, these models are high dimensional and difficult to analyze. Others have taken an alternative approach and developed low-dimensional models (e.g., Izhikevich, 2010). Although these reduced models often lack biophysical detail, they still manifest salient features of neuronal excitability (e.g., threshold behavior and excitability) and have provided some fundamental insights into excitability. Three of these reduced models will be described briefly.

The FitzHugh-Nagumo Model

Perhaps the best-known and most widely used low-dimensional model of an excitable system is the FitzHugh-Nagumo model (FitzHugh, 1961; Nagumo et al., 1962) (for reviews see Faghih et al., 2010, 2012; Koch, 1999; Murray, 1993; Rinzel, 1990). This model qualitatively describes the events occurring in an excitable membrane. The FitzHugh-Nagumo equations are often written, assuming dimensionless variables, in the general form:

$$\frac{dv}{dt} = f(v) - w + I_s \quad (14.66)$$

$$\frac{dw}{dt} = \phi(v - \gamma w) \quad (14.67)$$

where $f(v)$ is the cubic:

$$f(v) = v(1 - v)(v - a) \quad (14.68)$$

Here v corresponds to membrane potential, w is a recovery variable (i.e., combines the effects of h and n), which activates slowly (i.e., the rate constant, ϕ , is less than one) and γ is a positive constant. The cubic expression represents a nonlinear I-V relationship, which follows from the assumption that inward current activates instantaneously; a is the voltage threshold for this current. The qualitative behavior of FitzHugh-Nagumo is very similar to that of the HH system in that for some parameter regimes the model has a globally

stable resting state yet is excitable in that a sufficiently large perturbation will elicit a spike. The system does not have a saddle node, and thus manifests a pseudo-threshold, which is similar to the HH system (see Box 14.2). In addition, with sustained current injection, a limit cycle appears and the system oscillates. The simplicity of this model has made it a model of choice for nonlinear dynamical analyses of excitability and for simulations of large-scale networks of excitable elements.

The Morris-Lecar Model

The Morris-Lecar model (Morris and Lecar, 1981) was formulated and studied in the context of investigating electrical activity in barnacle muscle fibers. The model incorporates a voltage-gated Ca^{2+} current and a voltage-gated, delay-rectifier K^+ current; neither current inactivates. The Morris-Lecar equations are often written, assuming dimensionless variables, in the general form:

$$C \frac{dv}{dt} = I_s - \bar{g}_{\text{Ca}} m_{\infty}(v)(v - v_{\text{Ca}}) - \bar{g}_{\text{K}} w(v)(v - v_{\text{K}}) - \bar{g}_{\text{I}}(v - v_{\text{I}}) \quad (14.69)$$

$$\frac{dw}{dt} = \Phi \frac{w_{\infty}(v) - w}{\tau_w(v)} \quad (14.70)$$

where:

$$m_{\infty}(v) = 0.5 \left(1 + \tanh \frac{v - v_1}{v_2} \right) \quad (14.71)$$

$$w_{\infty}(v) = 0.5 \left(1 + \tanh \frac{v - v_3}{v_4} \right) \quad (14.72)$$

$$\tau_w(v) = \frac{1}{\cosh \frac{v - v_3}{v_4}} \quad (14.73)$$

where v_i are parameters, w is the fraction of K^+ channels open.

The qualitative behavior of the Morris-Lecar model is very similar to that of the HH system in that for some parameter regimes the model has a globally stable resting state yet is excitable. The system manifests a pseudo-threshold and oscillates with sustained current injection. The Morris-Lecar model has been studied extensively by Rinzel and Ermentrout (1998). They demonstrated an intriguing feature of this system. For some parameter regimes the oscillations emerge via a subcritical Hopf bifurcation (e.g., see Fig. 14.19). Thus, this two-dimensional system manifests bistability. Indeed, with different parameter regimes the two-variable system

BOX 14.5 (cont'd)

manifests tristability (i.e., two distinct stable steady states and a stable limit cycle coexist for a given parameter regime). The greatest advantage of the model has come from an expanded version which includes a third variable that describes the dynamics of intracellular Ca^{2+} , and by adding a Ca^{2+} -dependent K^+ current. This three-variable system can simulate a variety of bursting behaviors. The simplicity of this model and its rich dynamical repertoire make it an excellent choice for non-linear dynamical analyses of complex neuronal firing patterns such as bursting.

The Hindmarsh-Rose Model

Although similar to the FitzHugh-Nagumo model, the Hindmarsh-Rose model (Hindmarsh and Rose, 1982) was developed from first principles with the assumptions that the rate of change of membrane potential (dx/dt) depends linearly on z (an externally applied current) and y (an intrinsic current). The forms of the functions and values for the parameters were selected to fit data from a large neuron in the visceral ganglion of the pond snail *Lymnaea stagnalis*. The equations for this reduced model are:

$$\frac{dx}{dt} = -a(f(x) - y - z) \quad (14.74)$$

$$\frac{dy}{dt} = b(f(x) - q \exp(rx) + s - y) \quad (14.75)$$

where $f(x)$ is given by the cubic:

$$f(x) = cx^3 + dx^2 + ex + h \quad (14.76)$$

where $a-e$, h , q , r , and s are constants. This two-variable system offers some advantages, such as a better fit of the frequency-current relationship and a better fit to aspects of the spike waveform. As with the Morris-Lecar model, however, the greatest advantages of the Hindmarsh-Rose model have come from extended versions. A three-dimensional version (de Lange and Hasler, 2008; Hindmarsh and Rose, 1984; Rose and Hindmarsh, 1985, 1989a,b; Wang, 1993) manifests bursting activity and multistability, including multirhythmicity (i.e., multiple forms of bursting activity coexisting for a single parameter regime). Additional extensions of the model (Rose and Hindmarsh, 1989c) have been used to investigate the dynamical properties of thalamic neurons. Of the reduced models of excitability, the Hindmarsh-Rose model appears to exhibit the richest repertoire of dynamical properties.

which in turn reduces $I_{K, \text{Ca}}$ and oscillations return. This pattern of activity does not require an external stimulus and will continue indefinitely. Thus, this type of bursting behavior is that of an *endogenous burster*. This type of bursting activity has been observed in mesencephalic trigeminal sensory neurons (Pedroarena et al., 1999).

Although phase plane analysis cannot provide a full description for higher-order systems such as the three-variable model (i.e., Eqs. 14.49 and 14.50, and 14.64), judicious two-dimensional projections can yield useful insights into the dynamical behavior of higher-order systems. Canavier et al. (1993, 1994) provide an example of how a phase plane can be used to analyze an 11-order model of a bursting neuron. Figure 14.22A illustrates a bifurcation diagram for the three-variable model. To construct this diagram, the observation was made that the intracellular concentration of Ca^{2+} (i.e., Eq. 14.64) changed very slowly relative to the other state variables (i.e., $V_m(t)$ and $w(t)$). Thus, the function z , which is directly related to the intracellular concentration of Ca^{2+} (see Eq. 14.63), can be treated as a *parameter* (i.e., a bifurcation parameter) rather than as a *function* when analyzing the dynamics of V_m and w .

Because V_m and w are relatively fast as compared to $[\text{Ca}^{2+}]$ (and z), Eqs. 14.49 and 14.50 (i.e., the equations that describe V_m and w) are termed the fast subsystem and Eq. 14.64 (i.e., the equation that describes $[\text{Ca}^{2+}]$) is termed the slow subsystem. For each value of z , the dynamics of V_m and w can be analyzed. For some values of z , V_m and w may oscillate (i.e., spiking activity), whereas for other values of z , V_m and w may settle to a fixed point (i.e., quiescent membrane potential). As the magnitude of z is varied, the fast subsystem may undergo bifurcations where V_m and w are first at a fixed point and then begin to oscillate, or conversely, where V_m and w are oscillating and then become quiescent (see Fig. 14.22).

In Fig. 14.22A, the branch of the steady states (black line with stable steady states represented by a solid line and unstable steady states represented by a dashed line) forms the S-shaped curve and the oscillatory solutions are represented by the forked curve (yellow line with stable oscillatory states represented by a solid line and unstable oscillation represented by a dashed line). As the magnitude of z decreases (i.e., moving from right to left along the X-axis), the stable steady state destabilizes at a turning point (point HB at $z = 0.13$), which is subcritical Hopf bifurcation.

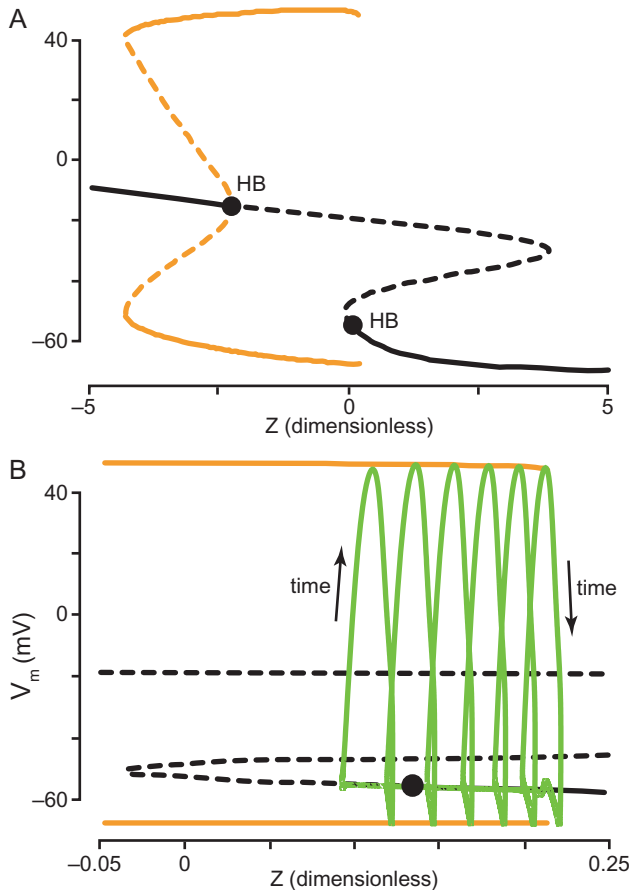


FIGURE 14.22 Bifurcation diagram of the three-dimensional system with z as the bifurcation parameter. Although z is a variable, it is sufficiently slow relative to changes in either $V_m(t)$ or $w(t)$, which constitute a fast subsystem, that it can be treated as a parameter for the purpose of generating this bifurcation analysis. **A:** Bifurcation diagram using z as the control parameter. As before, solid lines indicate stable solutions and dashed lines indicated unstable solutions. The black line indicates the steady states and yellow line indicates periodic solutions. From right to left (i.e., as the magnitude of z is decreased), the steady state loses stability via a subcritical Hopf bifurcation (point HB at $z = 0.13$). The unstable oscillations that are born at the subcritical Hopf bifurcation (see Fig. 14.20) terminate in a saddle loop (not shown) and a stable periodic solution emerges beyond the saddle-loop bifurcation. As the magnitude of z continues to decrease, the stable periodic solution destabilizes, and a stable steady state is re-established, again via a Hopf bifurcation (point HB at $z = -2.3$). **B:** Projection of the bursting solution in the $z - V_m$ phase plane (green line) onto the bifurcations diagram for positive values of z . Note the resolution of the bifurcation has been substantially increased. The direction of the solution path (i.e., time) is indicated by the arrows. The trajectory tracks the fast subsystem (i.e., spiking in the periodic solution) until it reaches the unstable regime. At which point, the trajectory “falls” onto the stable branch of the steady state. As intracellular levels of Ca^{2+} decrease (see Fig. 14.21B) and z decreases, the trajectory is forced past the point where the stable steady state disappears (black, filled circle). Once in this unstable regime, the trajectory “jumps” onto the stable branch of the periodic solution. Thus, bursting emerges as the slow subsystem (i.e., $z(t)$) forces the trajectory to slowly drift through bifurcations in the fast subsystem. With the exception of z , all values for parameters were as in Fig. 14.21.

The unstable oscillations born at this Hopf bifurcation, which are not illustrated, terminate in a saddle loop. A stable period solution emerges from this saddle loop bifurcation. As the magnitude of z continues to decrease, the stable periodic solutions destabilize, again via a subcritical Hopf bifurcation (point HB at $z = -2.3$), and a stable steady state is re-established. Although negative values of z are physiologically irrelevant, the bifurcation diagram serves to illustrate that the stable steady states of the three-variable model destabilize via subcritical Hopf bifurcations, and that for physiologically relevant values of z (i.e., $z \geq 0$), the stable periodic solutions disappear abruptly when they reach the saddle node of periodics (SNP). For more detailed explanations of this bifurcation diagram, see Chapter 6, Bertram et al. (1995), Rinzel and Ermentrout (1998), Izhikevich (2001), Canavier et al. (2002), and Qi et al. (2013).

The transitions between resting and oscillatory states can be visualized by projecting the burst solution in the $z - V$ plane onto the bifurcation diagram (Fig. 14.22B). The resolution of the bifurcation diagram has been increased to focus attention on the ranges of values for z that are observed during the bursting activity (see Fig. 14.21). The trajectory (red line) tracks the stable periodic solution (i.e., the fast subsystem) until it loses stability (i.e., at the SNP). During spiking activity, the levels of Ca^{2+} increase, and hence the magnitude of z also increases (see Eq. 14.63 and Fig. 14.21). Thus, the general movement of the trajectory along the stable branch of the periodic solution is from left to right. At the termination of the stable branch of the periodic solution (i.e., at the SNP), the trajectory then “falls” onto the stable branch of the steady state (i.e., a quiescent membrane potential). During the quiescent phase, the level of Ca^{2+} decreases, and hence the magnitude of z also decreases (see Fig. 14.21). The general movement of the trajectory along the stable branch of the steady state solution is from right to left. As z decreases (see Fig. 14.21B), the trajectory slowly moves through the Hopf bifurcation, and as the steady state loses stability, the trajectory “jumps” onto the stable branches of the periodic solution and the general movement of the trajectory once again is from left to right. Thus, the oscillations in the intracellular levels of Ca^{2+} , which in turn induce oscillations in z and $I_{K, \text{Ca}}$, drive the trajectory back and forth through the bifurcation between spiking and nonspiking.

The envelope of $V_m(t)$ during the burst activity of Fig. 14.21A is “elliptical” as the subthreshold oscillations gradually increase (i.e., wax) in amplitude before a burst and gradually decrease (i.e., wane) at the end of the burst. Thus, this type of bursting activity is often referred to as *elliptic bursting*. Other qualitative types of bursting have been observed, such as *parabolic*

bursting (i.e., the frequency of spiking activity gradually increases and then decreases during the burst) and *square-wave bursting* (i.e., the burst of spikes ride atop a plateau-like depolarization). Bursting activity can also be classified on the basis of the types of bifurcations that give rise to the oscillatory states. The history of formally classifying bursting began with Rinzel and Lee (1987), who contrasted the bifurcation mechanisms inherent in the elliptic, parabolic and square wave bursters. Bertram et al. (1995) suggested referring to the types of bursting using Roman numerals (i.e., elliptic bursting is Type I, parabolic bursting is Type II, and square-wave bursting is Type III). There are many ways that a nonlinear system can make a transition from a stable resting state to a stable periodic solution and there are many possible combinations. Izhikevich (2000) has described all possible combinations and reviewed examples of each.

SUMMARY

Some neurons are normally quiescent, but excitable in that they can fire one or more action potentials in response to transient stimuli. Others are capable of firing action potentials in a repetitive fashion in the absence of external stimuli. The same nonlinear properties of the cell membrane that allow a neuron to fire a single action potential can enable it to function as a nonlinear oscillator, generating sustained rhythmic activity. The simplest type of repetitive action potential firing is pacemaker activity in which single, apparently identical, action potentials are generated at relatively fixed intervals. Another type of rhythmic firing, bursting, is characterized by action potentials clustered into bursts that are separated by quiescent periods. To generate either an action potential or a sustained oscillation of any kind, two opposing processes are required, one relatively rapid autocatalytic process and one somewhat slower, restorative process. For rhythmic activity to be sustained, the opposing processes must have the appropriate steady-state characteristics and kinetics to continue to alternately dominate the system dynamics. In addition to the two processes required for action potential generation, a bursting oscillation requires at least one additional, slower process to modulate action potential firing so as to group them in bursts.

Acknowledgments

We thank Dr. C.C. Canavier for her assistance in the initial implementation of the reduced model and her comments on a previous version of this manuscript. We also thank Drs. E. Av-Ron and P. Smolen for their comments on a previous version of the manuscript.

References

- Abbott, L.F., 1994. Single neuron dynamics: an introduction. In: Ventriglia, F. (Ed.), *Neural Modeling and Neural Networks*. Pergamon Press, New York, NY, pp. 57–78.
- Abraham, R.H., Shaw, C.D., 1992. *Dynamics: The Geometry of Behavior*. Addison-Wesley Publishing Company, Redwood City, CA.
- Alexander, J.C., Cai, D.-Y., 1991. On the dynamics of bursting systems. *J. Math. Biol.* 29, 405–423.
- Av-Ron, E., 1994. The role of a transient potassium current in a bursting neuron model. *J. Math. Biol.* 33, 71–87.
- Av-Ron, E., Parnas, H., Segel, L., 1991. A minimal biophysical model for an excitable and oscillatory neuron. *Biol. Cybern.* 65, 487–500.
- Av-Ron, E., Parnas, H., Segel, L., 1993. A basic biophysical model for bursting neurons. *Biol. Cybern.* 69, 87–95.
- Baxter, D.A., Byrne, J.H., 2007. Simulator for neural networks and action potentials. In: Crasto, C.J. (Ed.), *Methods in Molecular Biology: Neuroinformatics*. Humana Press, Totowa, NJ, pp. 127–154.
- Bertram, R., 1994. Reduced-system analysis of the effects of serotonin on a molluscan burster neuron. *Biol. Cybern.* 70, 359–368.
- Bertram, R., Butte, M.J., Kiemel, T., Sherman, A., 1995. Topological and phenomenological classification of bursting oscillations. *Bull. Math. Biol.* 57, 413–439.
- Bezanilla, F., Armstrong, C.M., 1977. Inactivation of the sodium channel. I. Sodium current experiments. *J. Gen. Physiol.* 70, 549–566.
- Bower, J.M., Beeman, D., 1998. *The Book of GENESIS*. Springer-Verlag Publishers, New York, NY.
- Brette, R., Rudolph, M., Carnevale, T., Hines, M., Beeman, D., Bower, J.M., et al., 2007. Simulation of networks of spiking neurons: a review of tools and strategies. *J. Comput. Neurosci.* 23, 349–398.
- Brown, A.M., 1999. A methodology for simulating biological systems using Microsoft EXCEL. *Comput. Methods Programs Biomed.* 58, 181–190.
- Brown, A.M., 2000. Simulation of axonal excitability using a spreadsheet template created in Microsoft EXCEL. *Comput. Methods Programs Biomed.* 63, 47–54.
- Butera, R.J., 1998. Multirhythmic bursting. *Chaos*, 8, 274–284.
- Butera, R.J., Clark, J.W., Byrne, J.H., 1996. Dissection and reduction of a modeled bursting neuron. *J. Comput. Neurosci.* 3, 199–223.
- Byrne, J.H., Schultz, S.G., 1994. *An Introduction to Membrane Transport and Bioelectricity*. Raven Press, New York, NY.
- Canavier, C.C., Clark, J.W., Byrne, J.H., 1991. Simulation of the bursting activity of neuron R15 in *Aplysia*: role of ionic currents, calcium balance, and modulatory transmitters. *J. Neurophysiol.* 66, 2107–2124.
- Canavier, C.C., Baxter, D.A., Clark, J.W., Byrne, J.H., 1993. Nonlinear dynamics in a model neuron provide a novel mechanism for transient synaptic inputs to produce long-term alterations of postsynaptic activity. *J. Neurophysiol.* 69, 2252–2257.
- Canavier, C.C., Baxter, D.A., Clark, J.W., Byrne, J.H., 1994. Multiple modes of activity in a model neuron suggest a novel mechanism for the effects of neuromodulators. *J. Neurophysiol.* 72, 872–882.
- Canavier, C.C., Baxter, D.A., Byrne, J.H., 2002. Repetitive action potential firing. In: Group, N.P. (Ed.), *Encyclopedia of Life Sciences*. Grove's Dictionaries, New York, NY, online <<http://www.els.net>>.
- Catterall, W.A., Raman, I.M., Robinson, H.P.C., Sejnowski, T.J., Paulsen, O., 2012. The Hodgkin-Huxley heritage: from channels to circuits. *J. Neurosci.* 32, 14064–14073.
- Clay, J.R., 1998. Excitability of squid giant axon revisited. *J. Neurophysiol.* 80, 903–913.
- Clay, J.R., Paydarfar, D., Forger, D.B., 2008. A simple modification of the Hodgkin and Huxley equations explains type 3 excitability in squid giant axons. *J. R. Soc. Interface* 5, 10.1098/rsif.2008.0166.

- Cole, K.S., 1949. Dynamic electrical characteristics of the squid axon membrane. *Arch. Sci. Physiol.* 22, 253–258.
- Cole, K.S., 1968. *Membranes, Ions, and Impulses*. University of California Press, Berkeley, CA.
- Cole, K.S., Antosiewicz, H.A., Rabinowitz, P., 1955. Automatic computation of nerve excitation. *J. Soc. Indust. Appl. Math.* 3, 153–172.
- Cole, K.S., Guttman, R., Bezanilla, F., 1970. Nerve excitation without threshold. *Proc. Natl. Acad. Sci. USA* 65, 884–891.
- Cooke, I., Lipkin, M. (Eds.), 1972. *Cellular Neurophysiology: A Source Book*. Holt, Rinehart and Winston, Inc., New York, NY.
- Cronin, J., 1987. *Mathematical Aspects of Hodgkin-Huxley Neural Theory*. Cambridge University Press, New York, NY.
- Dayan, P., Abbott, L.F., 2001. *Theoretical Neuroscience: Computational and Mathematical Modeling of Neural Systems*. The MIT Press, Cambridge, MA.
- De Lange, E., Hasler, M., 2008. Predicting single spikes and spike patterns with the Hindmarsh-Rose model. *Biol. Cybern.* 99, 349–360.
- DeSchutter, E., 1989. Computer software for development and simulation of compartmental models of neurons. *Comput. Biol. Med.* 19, 71–81.
- DeSchutter, E., 1992. A consumer guide to neuronal modeling software. *Trends Neurosci.* 15, 462–464.
- DeSchutter, E. (Ed.), 2001. *Computational Neuroscience: Realistic Modeling for Experimentalists*. CRC Press, New York, NY.
- Dodge, F., Frankenhaeuser, B., 1959. Sodium currents in the myelinated nerve fibre of *Xenopus laevis* investigated with the voltage clamp technique. *J. Physiol. (Lond.)* 148, 188–200.
- Doedel, E.J., 1981. AUTO: a program for the automatic bifurcation and analysis of autonomous systems. *Cong. Num.* 30, 265–284.
- Drion, G., Franci, A., Seutin, V., Sepulchre, R., 2012. A novel phase portrait of neuronal excitability. *PLoS ONE* 7 (8), e41806.
- Ermentrout, G.B., 1996. Type I membranes, phase resetting curves, and synchrony. *Neural Comp.* 8, 979–1001.
- Ermentrout, G.B., 2002. *Simulating, Analyzing and Animating Dynamical Systems: A Guide to XPPAUT for Researchers and Students*. SIAM, Philadelphia, PA.
- Faghih, R.T., Savla, K., Dahleh, M.A., Brown, E.N., 2010. The FitzHugh-Nagumo model: firing modes with time-varying parameters & parameter estimation. *Conf. Proc. IEEE Eng. Med. Soc.* 2010, 4116–4119.
- Faghih, R.T., Savla, K., Dahleh, M.A., Brown, E.N., 2012. Broad range of neural dynamics from a time-varying FitzHugh-Nagumo model and its spiking threshold estimation. *IEEE Trans. Biomed. Eng.* 59, 816–823.
- FitzHugh, R., 1960. Thresholds and plateaus in the Hodgkin-Huxley equations. *J. Gen. Physiol.* 43, 867–896.
- FitzHugh, R., 1961. Impulses and physiological states in theoretical models of nerve membrane. *Biophys. J.* 1, 445–466.
- FitzHugh, R., 1966. Theoretical effects of temperature on threshold in the Hodgkin-Huxley nerve model. *J. Gen. Physiol.* 49, 989–1005.
- FitzHugh, R., 1969. Mathematical models of excitation and propagation in nerve. In: Schwan, H.P. (Ed.), *Biological Engineering*. McGraw-Hill Book Company, New York, NY, pp. 1–85.
- FitzHugh, R., Antosiewicz, H.A., 1959. Automatic computation of nerve excitation—detailed correction and addition. *J. Soc. Indust. Appl. Math.* 7, 447–458.
- Gall, W.G., Zhou, Y., 2000. An organizing center for planar neural excitability. *Neurocomp.* 32–33, 757–765.
- Guttman, R., Lewis, S., Rinzel, J., 1980. Control of repetitive firing in squid axon membrane as a model for a neurone oscillator. *J. Physiol. (Lond.)* 305, 377–395.
- Hayes, R., Byrne, J.H., Baxter, D.A., 2002. *Neurosimulation: tools and resources*. In: Arbib, M.A. (Ed.), *The Handbook of Brain Theory and Neural Networks*. MIT Press, Cambridge, MA, pp. 776–780.
- Hille, B., 2001. *Ionic Channels of Excitable Membranes*. Sinauer Associates, Inc., Sunderland.
- Hindmarsh, J., Rose, R.M., 1984. A model of neuronal bursting using three coupled first order differential equations. *Proc. R. Soc. Lond. B* 221, 87–102.
- Hindmarsh, J.L., Rose, R.M., 1982. A model of the nerve impulse using two first-order differential equations. *Science* 296, 162–164.
- Hines, M.L., Carnevale, N.T., 1997. The NEURON simulation environment. *Neural Comput.* 9, 1179–1209.
- Hodgkin, A.L., 1964. The ionic basis of nervous conduction. *Science* 145, 1148–1154.
- Hodgkin, A.L., 1976. Chance and design in electrophysiology: an informal account of certain experiments on nerve carried out between 1934 and 1952. *J. Physiol. (Lond.)* 263, 1–21.
- Hodgkin, A.L., 1977. *The Pursuit of Nature: Informal Essays on the History of Physiology*. Cambridge University Press, Cambridge, UK.
- Hodgkin, A.L., Huxley, A.F., 1952a. Currents carried by sodium and potassium ions through the membrane of the giant axon of *Loligo*. *J. Physiol. (Lond.)* 116, 449–472.
- Hodgkin, A.L., Huxley, A.F., 1952b. The components of membrane conductance in the giant axon of *Loligo*. *J. Physiol. (Lond.)* 116, 473–496.
- Hodgkin, A.L., Huxley, A.F., 1952c. The dual effect of membrane potential on sodium conductance in the giant axon of *Loligo*. *J. Physiol. (Lond.)* 116, 497–506.
- Hodgkin, A.L., Huxley, A.F., 1952d. A quantitative description of membrane current and its application to conduction and excitation in nerve. *J. Physiol. (Lond.)* 117, 500–544.
- Hodgkin, A.L., Huxley, A.F., 1990. A quantitative description of membrane current and its application to conduction and excitation in nerve. 1952. *Bull. Math. Biol.* 52, 5–23.
- Hodgkin, A.L., Huxley, A.F., Katz, B., 1952. Measurements of current-voltage relations in the membrane of the giant axon of *Loligo*. *J. Physiol. (Lond.)* 116, 424–448.
- Hoppensteadt, F., 2013. Heuristics for the Hodgkin-Huxley system. *Math. Biosci.* 24, 56–60.
- Hoppensteadt, F., Izhikevich, E., 2001. Canonical neural models. In: Arbib, M.A. (Ed.), *Brain Theory and Neural Networks*. The MIT Press, Cambridge, MA, pp. 1–7.
- Huang, C.L.-H., 2012. Andrew Fielding Huxley (1917–2012). *J. Physiol. (Lond.)* 590, 3415–3420.
- Hubbard, J.H., West, B.H., 1992. *MacMath: A Dynamical Systems Software Package for the Macintosh*. Springer, New York, NY.
- Huxley, A.F., 1951. The ionic basis of electrical activity in nerve and muscle. *Biol. Rev.* 26, 339–409.
- Huxley, A.F., 1959. Can a nerve propagate a subthreshold disturbance? *J. Physiol. (Lond.)* 148, 80–81P.
- Huxley, A.F., 1964. Excitation and conduction in nerve: quantitative analysis. *Science* 145, 1154–1159.
- Huxley, A.F., 2000. Reminiscences: working with Alan, 1939–1952. *J. Physiol. (Lond.)* 527P, 13S.
- Huxley, A.F., 2002. Hodgkin and the action potential, 1939–1952. *J. Physiol. (Lond.)* 538, 2.
- Izhikevich, E.M., 2000. Neural excitability, spiking and bursting. *Int. J. Bifurcation Chaos* 10, 1171–1266.
- Izhikevich, E.M., 2001. Synchronization of elliptic bursters. *SIAM Rev.* 43, 315–344.
- Izhikevich, E.M., 2010. Hybrid spiking models. *Philos. Trans. A. Math. Phys. Eng. Sci.* 368, 5061–5070.
- Jackson, E.A., 1991. *Perspectives of Nonlinear Dynamics*. Cambridge University Press, Cambridge, UK.
- Johnston, D., Wu, S.M., 1997. *Foundations of Cellular Neurophysiology*. The MIT Press, Cambridge, MA.
- Kepler, T.B., Abbott, L.F., Marder, E., 1992. Reduction of conductance-based neuron models. *Biol. Cybern.* 66, 381–387.

- Kirsch, R.A., 1998. SEAC and start of image processing at the National Bureau of Standards. *IEEE Ann. History Comput.* 20, 7–13.
- Kocak, H., 1989. *Differential and Difference Equations through Computer Experiments*, second ed. Springer, New York, NY.
- Koch, C., 1999. *Biophysics of Computation: Information Processing in Single Neurons*. Oxford University Press, New York, NY.
- Lechner, H.A., Baxter, D.A., Clark, J.W., Byrne, J.H., 1996. Bistability and its regulation by serotonin in the endogenously bursting neuron R15 in *Aplysia*. *J. Neurophysiol.* 75, 957–962.
- MacGregor, R.J., 1987. *Neural and Brain Modeling*. Academic Press, Inc., New York, NY.
- Marmont, G., 1949. Studies on the axon membrane. I. A new method. *J. Cell. Comp. Physiol.* 34, 351–382.
- McCormick, D.A., Huguenard, J., 1992. A model of the electrophysiological properties of thalamocortical relay neurons. *J. Neurophysiol.* 68, 1384–1440.
- Moore, J.W., 2010. A personal view of the early development of computational neuroscience in the USA. *Front. Comput. Neurosci.* 4, 20.
- Moore, J.W., Stuart, A.E., 2000. *Neurons in Action: Computer Simulations with NeuroLab*. Sinauer Associates, Inc. Publishers, Sunderland, MA.
- Morris, C., Lecar, H., 1981. Voltage oscillations in the barnacle giant muscle fiber. *Biophys. J.* 35, 193–213.
- Murray, J.D., 1993. *Mathematical Biology*. Springer, New York, NY.
- Nagumo, J.S., Arimoto, S., Yoshizawa, S., 1962. An active pulse transmission line simulating a nerve axon. *Proc. IRE.* 50, 2061–2070.
- Nelson, M., Rinzel, J., 1998. The Hodgkin-Huxley model. In: Bower, J.M., Beeman, D. (Eds.), *The Book of GENESIS: Exploring Realistic Neural Models with the GENeral NEural SIMulation System*. Springer-Verlag, New York, NY, pp. 29–49.
- Nelson, M.E., 2011. Electrophysiological models of neural processing. *Wiley Interdiscip. Rev. Syst. Biol. Med.* 3 (1), 74–92. 10.1002/wsbm.95.
- Palti, Y., 1971a. Description of axon membrane ionic conductances and currents. In: Adelman, W.J. (Ed.), *Biophysics and Physiology of Excitable Membrane*. Van Nostrand Reinhold Company, New York, NY, pp. 168–182.
- Palti, Y., 1971b. Digital computer solutions of membrane currents in the voltage clamped giant axon. In: Adelman, W.J. (Ed.), *Biophysics and Physiology of Excitable Membranes*. Van Nostrand Reinhold Company, New York, NY, pp. 183–193.
- Pavlidis, T., 1973. *Biological Oscillators: Their Mathematical Analysis*. Academic Press, New York, NY.
- Pedroarena, C.M., Pose, I.E., Yamuy, J., Chase, M.H., Morales, F.R., 1999. Oscillatory membrane potential activity in the soma of a primary afferent neuron. *J. Neurophysiol.* 82, 1465–1476.
- Pospichil, M., Toledo-Rodriguez, M., Monier, C., Piwkowska, Z., Bal, T., Fregnac, Y., et al., 2008. Minimal Hodgkin-Huxley type models for different classes of cortical and thalamic neurons. *Biol. Cybern.* 99, 427–441. 10.1007/s00422-008-0263-8.
- Qi, Y., Wats, A.L., Kim, J.W., Robinson, P.A., 2013. Firing patterns in a conductance-based neuron model: bifurcation, phase diagram, and chaos. *Biol. Cybern.* 107, 15–24.
- Rinzel, J., 1985. Excitation dynamics: insights from simplified membrane models. *Fed. Proc.* 44, 2944–2946.
- Rinzel, J., 1990. Electrical excitability of cells, theory and experiment: review of the Hodgkin-Huxley foundation and an update. *Bull. Math. Biol.* 52, 5–23.
- Rinzel, J., 1998. The Hodgkin-Huxley model. In: Bower, J.M., Beeman, D. (Eds.), *The Book of Genesis: Exploring Realistic Neural Networks with the GENeral NEural SIMulation System*. Springer-Verlag, New York, NY, pp. 251–292.
- Rinzel, J., Ermentrout, G.B., 1998. Analysis of neural excitability and oscillations. In: Koch, C., Segev, I. (Eds.), *Methods in Neuronal Modeling: From Ions to Networks*, second ed. The MIT Press, Cambridge, MA, pp. 251–292.
- Rinzel, J., Lee, Y.S., 1987. Dissection of a model for neuronal parabolic bursting. *J. Math. Biol.* 25, 653–675.
- Rose, R.M., Hindmarsh, J.L., 1985. A model of a thalamic neuron. *Proc. R. Soc. Lond. B.* 225, 161–193.
- Rose, R.M., Hindmarsh, J.L., 1989a. The assembly of ionic currents in a thalamic neuron I. The three-dimensional model. *Proc. R. Soc. Lond. B.* 237, 267–288.
- Rose, R.M., Hindmarsh, J.L., 1989b. The assembly of ionic currents in a thalamic neuron II. The stability and state diagrams. *Proc. R. Soc. Lond. B.* 237, 289–312.
- Rose, R.M., Hindmarsh, J.L., 1989c. The assembly of ionic current in a thalamic neuron III. The seven-dimensional model. *Proc. R. Soc. Lond. B.* 237, 313–334.
- Schwiening, C.J., 2012. A brief historical perspective: Hodgkin and Huxley. *J. Physiol. (Lond.)* 590, 2571–2575.
- Strogatz, S.H., 1994. *Nonlinear Dynamics and Chaos: With Applications to Physics, Biology, Chemistry and Engineering*. Perseus Books, Reading.
- Tuckwell, H.C., 1988. *Introduction to Technical Neurobiology: Volume 2: Nonlinear and Stochastic Theories*. Cambridge University Press, Cambridge, UK.
- Tufillaro, N.B., Abbott, T., Reilly, J., 1992. *An Experimental Approach to Nonlinear Dynamics and Chaos*. Addison-Wesley Publishing Company, Redwood City, CA.
- Vandenberg, C.A., Bezanilla, F., 1991. A sodium gating model based on single channel, macroscopic ionic, and gating currents in the squid giant axon. *Biophys. J.* 60, 511–533.
- Vandenberg, J.I., Waxman, S.G., 2012. Hodgkin and Huxley and the basis for electrical signalling: a remarkable legacy still going strong. *J. Physiol. (Lond.)* 590, 2569–2570.
- Ventriglia, F. (Ed.), 1994. *Neural Modeling and Neural Networks*. Pergamon Press, New York, NY.
- Wang, X.-J., 1993. Genesis of bursting oscillations in the Hindmarsh-Rose model and homoclinicity to a chaotic saddle. *Physica D.* 62, 263–274.
- Weiss, T.F., 1997. *Cellular Biophysics. Volume 2: Electrical Properties*. The MIT Press, Cambridge, MA.
- Wheeler, D.J., 1992a. The EDSAC programming systems. *IEEE Ann. History Comput.* 14, 34–40.
- Wheeler, J., 1992b. Applications of the EDSAC. *IEEE Ann. History Comput.* 14, 27–33.
- Ziv, I., Baxter, D.A., Byrne, J.H., 1994. Simulator for neural networks and action potentials: description and application. *J. Neurophysiol.* 71, 294–308.